Politechnika Warszawska

WYDZIAŁ FIZYKI

Master's diploma thesis

in the field of study Applied Physics
and specialization in Nuclear Physics and Technology

Investigating the mechanism of hadron production by measuring angular correlations of mesons with hidden strangeness in the ALICE experiment

Zuzanna Chochulska
student record book number: 305000

thesis supervisor:
Ph.D. D.Sc. Eng. Łukasz Graczykowski

CERN-THESIS-2024-009
02/02/2024

WARSZAWA 2024

I would like to thank my supervisor, Ph.D. D.Sc. Eng. Łukasz Graczykowski, for all the answers to my many questions and constant support. I would also like to thank everyone who made my Master's degree so special. Especially the ALICE WUT group, my lecturers and my friends. Finally, I would like to thank you, Filip, for being my constant support throughout this adventure.

Streszczenie

Tytuł pracy: Badanie mechanizmu produkcji hadronów poprzez pomiar korelacji kątowych mezonów o ukrytej dziwności w eksperymencie ALICE.

Hadronizacja to proces opisywany przez chromodynamikę kwantową, w którym z kwarków i gluonów powstają hadrony. Ze względu na nieperturbacyjną naturę tego zjawiska nie został on jeszcze w pełni poznany. Do badań tego efektu możemy używać jedynie modeli fenomenologicznych. Modele fenomenologiczne charakteryzują się tym, że parametry wykorzystywane do ich opisu otrzymuje się z danych doświadczalnych. Pierwsze próby modelowania tego procesu w zderzeniach cząstek można znaleźć już w 1977, ale badania tego zjawiska trwają do dzisiaj.

Korelacje kątowe to narzędzie, które pozwala na badanie fizyki ciężkich jonów, jak i lżejszych układów, w tym protonów. Korelacje funkcji $\Delta\eta$ oraz $\Delta\varphi$ (odpowiednio różnicy pseudopospieszności i kąta azymutalnego) wrażliwe są na wkłady pochodzące z różnych efektów fizycznych. Celem analiz jest wnioskowanie wpływów konkretnych efektów fizycznych na ostateczną funkcję korelacji kątowej. Dzięki symulacjom posiadamy wiedzę o tym jakich kształtów w przestrzeni ($\Delta\eta$, $\Delta\varphi$) możemy się spodziewać od poszczególnych efektów fizycznych.

Ze względu na możliwości identyfikacji cząstek eksperyment ALICE jest idealnym narzędziem do przeprowadzania analiz korelacji dla różnych cząstek. Po gruntownych zmianach wprowadzonych w systemie detektorów eksperymentu ALICE, konieczne było wprowadzenie nowego oprogramowania do analizy danych – ALICE O^2. Wraz ze zmianą software do analizy zmienił się również format danych i proces ich przetwarzania. Poprzez wykorzystanie płaskich tablic Appache Arrow, deklaratywnych metod programowania oraz języka C++ 17, pozwala na zmniejszenie wykorzystywanych zasobów oraz przyspieszenie czasu wykonywanych analiz.

Dotychczasowe badania prowadzone w dziedzinie korelacji kątowych wskazują, że proces hadronizacji barionów może przebiegać inaczej niż proces produkcji mezonów. W swojej pracy magisterskiej chciałabym odpowiedzieć na pytanie czy masa ma wpływ na proces hadronizacji, poprzez analizowanie korelacji kątowych mezonów o zbliżonej masie do najlżejszego barionu, jakim jest proton.

Słowa kluczowe:
CERN, ALICE, korelacje kątowe, hadronizacja, O2, mezon Phi

(czytelny podpis opiekuna naukowego) (czytelny podpis dyplomanta)

Abstract

Thesis title: Investigating the mechanism of hadron production by measuring angular correlations of mesons with hidden strangeness in the ALICE experiment

Hadronization is a process described by quantum chromodynamics in which hadrons are formed from quarks and gluons. Given the non-perturbative nature of this phenomenon, it is not yet fully understood. To study this effect, we can only use phenomenological models. Such phenomenological models are characterized by the fact that the parameters used to describe them are obtained from experimental data. Initial attempts to model this process in particle collisions can be found as early as 1977, but the study of this phenomenon continues to this day.

The angular correlations are a powerful tool for studying the physics of heavy ions as well as lighter systems, such as protons. The correlations of the functions $\Delta\eta$ and $\Delta\varphi$ (the difference in pseudorapidity and azimuthal angle, respectively) are sensitive to contributions from various physical effects. The purpose of the analyses is to derive the influences of specific physical effects on the final angular correlation function. Using simulations, we have knowledge of what shapes in space ($\Delta\eta$, $\Delta\varphi$) we can expect from particular physical effects.

In terms of its particle identification capabilities, the ALICE experiment is an ideal tool for performing correlation analyses for different particles. Following the extensive changes made to the ALICE experiment's detector system, it was necessary to introduce new data analysis software – ALICE O^2. Along with the change in the analysis software, the format of the data and its processing have also changed. Thanks to the use of Appache Arrow flat arrays, declarative programming methods and the C++ 17 language, it allows for a reduction in the resources used and a speeding up of the analysis time.

The existing research conducted in the field of angular correlations indicates that the process of hadronization of baryons may proceed differently from the process of meson production. This thesis intends to answer the question of whether mass affects the hadronization process by analyzing the angular correlations of mesons with similar mass to the lightest baryon, which is a proton.

Keywords
CERN, ALICE, angular correlations, hadronization, O2, Phi meson

(czytelny podpis opiekuna naukowego) (czytelny podpis dyplomanta)

Oświadczenie o samodzielności wykonania pracy

Politechnika Warszawska

Zuzanna Chochulska
305000
Fizyka Techniczna

Oświadczenie

Świadoma odpowiedzialności karnej za składanie fałszywych zeznań oświadczam, że niniejsza praca dyplomowa została napisana przeze mnie samodzielnie, pod opieką kierującego pracą dyplomową.

Jednocześnie oświadczam, że:

- niniejsza praca dyplomowa nie narusza praw autorskich w rozumieniu ustawy z dnia 4 lutego 1994 roku o prawie autorskim i prawach pokrewnych (Dz.U. z 2006 r. Nr 90, poz. 631 z późn. zm.) oraz dóbr osobistych chronionych prawem cywilnym,
- niniejsza praca dyplomowa nie zawiera danych i informacji, które uzyskałam w sposób niedozwolony,
- niniejsza praca dyplomowa nie była wcześniej podstawą żadnej innej urzędowej procedury związanej z nadawaniem dyplomów lub tytułów zawodowych,
- wszystkie informacje umieszczone w niniejszej pracy, uzyskane ze źródeł pisanych i elektronicznych, zostały udokumentowane w wykazie literatury odpowiednimi odnośnikami,
- znam regulacje prawne Politechniki Warszawskiej w sprawie zarządzania prawami autorskimi i prawami pokrewnymi, prawami własności przemysłowej oraz zasadami komercjalizacji.

Warszawa, dnia 20.01.2024 r.

(czytelny podpis dyplomanta)

Oświadczenie o udzieleniu Uczelni licencji do pracy

Politechnika Warszawska

Zuzanna Chochulska
305000
Fizyka Techniczna

Oświadczam, że jako autor pracy dyplomowej pt. *Badanie mechanizmu produkcji hadronów poprzez pomiar korelacji kątowych mezonów o ukrytej dziwności w eksperymencie ALICE* udzielam Politechnice Warszawskiej nieodpłatnej licencji na niewyłączne, nieograniczone w czasie, umieszczenie pracy dyplomowej w elektronicznych bazach danych oraz udostępnianie pracy dyplomowej w zamkniętym systemie bibliotecznym Politechniki Warszawskiej osobom zainteresowanym.

Licencja na udostępnienie pracy dyplomowej nie obejmuje wyrażenia zgody na wykorzystywanie pracy dyplomowej na żadnym innym polu eksploatacji, w szczególności kopiowania pracy dyplomowej w całości lub w części, utrwalania w innej formie czy zwielokrotniania.

Warszawa, dnia 20.01.2024r. (czytelny podpis dyplomanta)

Contents

Chapter 1

Introduction

Particle physics allows us to understand the state of matter immediately after the Big Bang. It makes it possible to try to better understand the processes that formed the world as we know it today. Hadronization is the process of hadron formation from coloured partons and is described by Quantum Chromodynamics (QCD) [1].

The mechanism of hadron production is not amenable to description in perturbative quantum mechanics, so phenomenological models are used. Those models are based on a theoretical framework that attempts to reflect what can be observed in the experimental data. The ultimate goal in particle physics is to derive physical phenomena from fundamental principles. Phenomenological models are intermediate tools to bridge the gap between empirical data and theory. They can be divided into two groups: macroscopic and microscopic models. Macroscopic models statistically describe a multi-particle system. We distinguish thermodynamic, statistical, and hydrodynamic macroscopic models. In contrast, microscopic models follow the fate of individual particles.

The first studies of the hadron production process date back to 1977, when R. Feynmann and R. Field proposed the first models for the production of so-called "jets", i.e. a collimated stream of particles [2]. This model represented the principles of how particles are created, how energy is distributed and what limitations emerge from conservation principles. According to the Feynman model of quark jets, the idea of ranks is being used to describe the hierarchy of final hadrons formed when a quark decays into hadrons. The primary mesons formed in this process are assigned ranks based on their relationship to the original quark. A primary hadron that contains the original quark is said to have a "rank of one," while subsequent primary mesons have higher ranks. Thus, a primary hadron's rank determines its decay products' rank. It should be noted, however, that the rank order in the hierarchy is not the same as the order in terms of momentum or velocity.

The principles outlined at the time are used even today in many fragmentation models. One of them, and arguably the most famous microscopic model is the Lund string model. A string is referred to as a quark-antiquark or quark-diquark pair bound by the colour field. The Lund string fragmentation model is implemented in the widely used PYTHIA event generator [3] in the field of particle physics, which is widely used in the modelling of the hadronization process. Figure 1.1 represents a schematic of the structure of a pp $\rightarrow$ tt event, as modelled by PYTHIA.

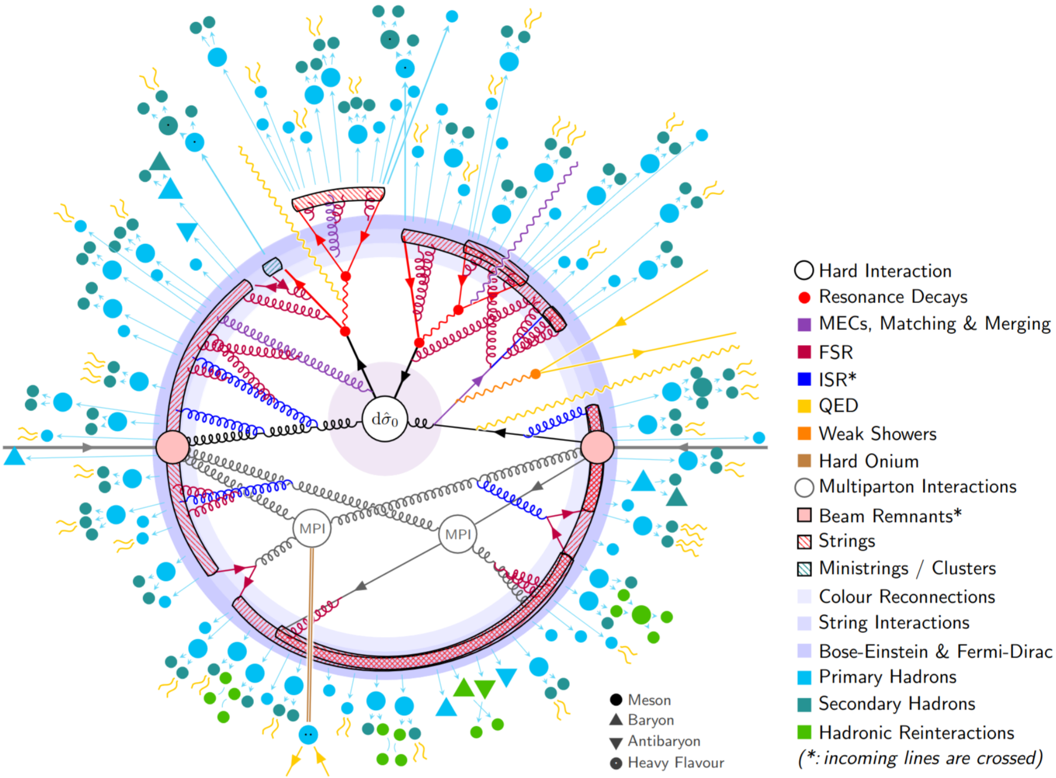

Figure 1.1: Schematic of the structure of a pp $\rightarrow$ tt event, as modelled by PYTHIA [3].

The two mechanisms contributing to baryon production are the popcorn and diquark models. PYTHIA model uses Lund fragmentation to simulate inelastic nucleon-nucleon collisions. When the string breaks, a pair of quarks is formed that have different colours to the initial pair. As a result, changes in the colour field manifest themselves. This process can result in meson or baryon-antibaryon production [4]. Thus, this is a more general model of baryon production. The diquark model assumes diquark production upon string breaking. If a string of quark and antiquark is found in the vicinity a baryon-antibaryon pair can be produced.

The string model described above is one of the three basic models that are used to describe the hadronization process. Furthermore, we also distinguish between independent fragmentation (ISAJET [5]) and clustered hadronization (HERWIG [6]).

The process of hadronization is studied with many different tools. This is made possible by a large number of physical experiments in a wide range of energies and systems all over the world. Researchers from the Faculty of Physics at Warsaw University of Technology contributed to this research. Research by the group working on the ALICE experiment done in 2017 [7] has shown that baryons produce themselves in a different way than currently used phenomenological models predict. Angular correlations were used to measure this effect using the data from pp collisions at $\sqrt{s_{NN}} = 7$ TeV. Figure 1.2 shows projections of angular correlations of selected hadron pairs on the difference in pseudorapidity $\Delta\eta$ axis. Those correlations will be further explained in later chapters of this thesis.

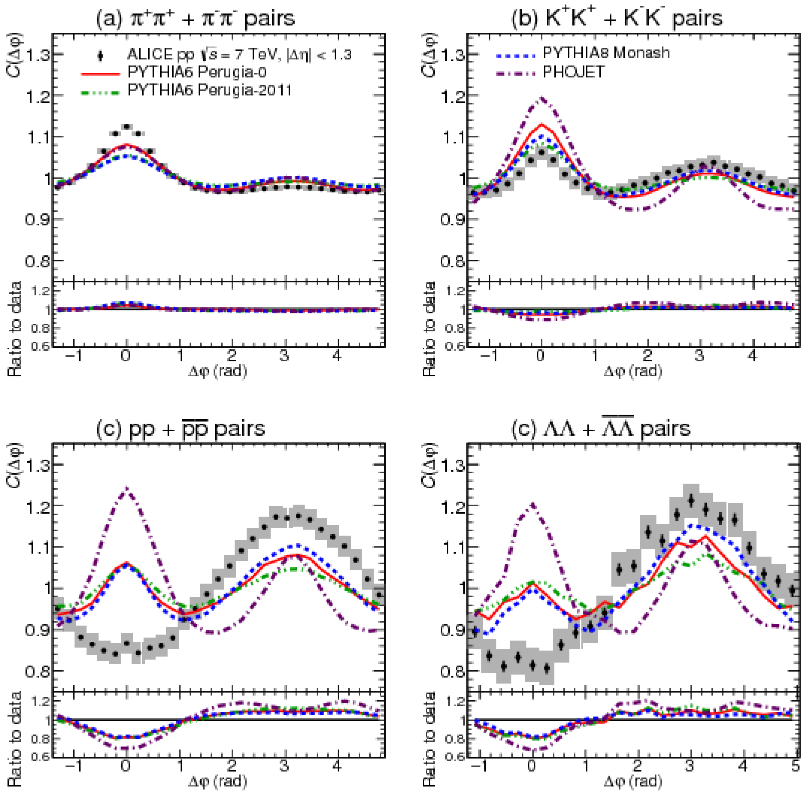

Figure 1.2: $\Delta\eta$ projections of correlation functions of (a) $\pi^+\pi^+ + \pi^-\pi^-$ (b) $K^+K^+ + K^-K^-$ (c) $\mathrm{pp} + \bar{\mathrm{p}}\bar{\mathrm{p}}$ (d) $\Lambda\Lambda + \bar{\Lambda}\bar{\Lambda}$ pairs in ALICE pp collisions at $\sqrt{s_{\mathrm{NN}}} = 7$ TeV [7].

From the obtained graphs we can conclude that for π mesons and kaons we observe that the data points are well reproduced by the models used. However, an analysis of the results obtained for the correlation of protons and lambdas reveals an apparent anti-correlation that is not predicted by any of the theoretical models tested. This may lead to the conclusion that the fragmentation mechanisms in the PYTHIA and PHOJET model may be incomplete, or that there may be some yet unrecognized mechanism for baryon production.

The observed effect is seen for both small and large systems. Similar observations have also been made in 2014 using data from the STAR experiment at energies from $\sqrt{s_{\mathrm{NN}}} = 7.7,$ GeV to $\sqrt{s_{\mathrm{NN}}} = 200,$ GeV in Au–Au collisions [8]. The two-particle correlations used for this purpose confirm the existence of an anticorrelation for correlations of particles with the same baryon number. Furthermore, the observed anticorrelation decreases with increasing beam energy and centrality and is p_{T} independent. This can be seen in figure 1.3, which shows the angular correlation function $R_2(\Delta y, \Delta\varphi)$ of (a) like-sign protons and (b) unlike-sign protons in Au–Au collisions at mid-centrality 30% – 40% and $0.4 < p_{\mathrm{T}} < 2.0\,\mathrm{GeV}/c$ in different beam energies from 7.7 GeV (top left) to 200 GeV (bottom right).

The topic of anticorrelation appearing in angular correlations for baryon-baryon and antibaryon-antibaryon pairs was also highlighted by one of the main authors of the PYTHIA generator – Prof. Torbjörn Sjöstrand – at the 2018 Quark Matter conference. From his proceedings [9],

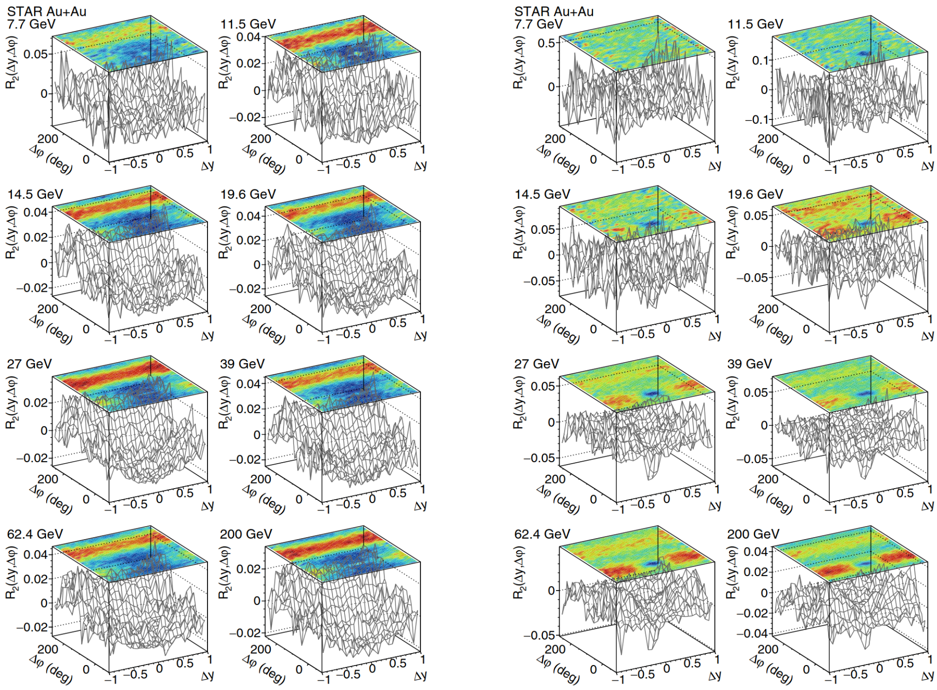

(a) Like-sign protons (b) Unlike-sign protons

Figure 1.3: Angular correlation function $R_2(\Delta y, \Delta\varphi)$ of (a) like-sign protons and (b) unlike-sign protons in Au + Au collisions at mid centrality 30% – 40% and $0.4 < p_T < 2.0$ GeV/c in different beam energies from 7.7 GeV (top left) to 200 GeV (bottom right). Due to the large statistical fluctuations in large Δy bins, the plots are presented in the range of $|\Delta y| \leq 1$ [8].

we read that *it is clear that we still lack some fundamental insights into baryon production, at least in the context of strings*. He also emphasizes that current models still struggle to give a good description of baryon production.

In 2019, the analysis from paper [7] was repeated on $\sqrt{s_{NN}} = 13$ TeV data. Figure 1.4 shows still preliminary $\Delta\eta$ projections of angular correlation functions for like-sign pairs of pions, kaons and protons. This result confirms that as the collision energy increases, we continue to observe the same anti-correlation effect for proton-proton and antiproton-antiproton pairs.

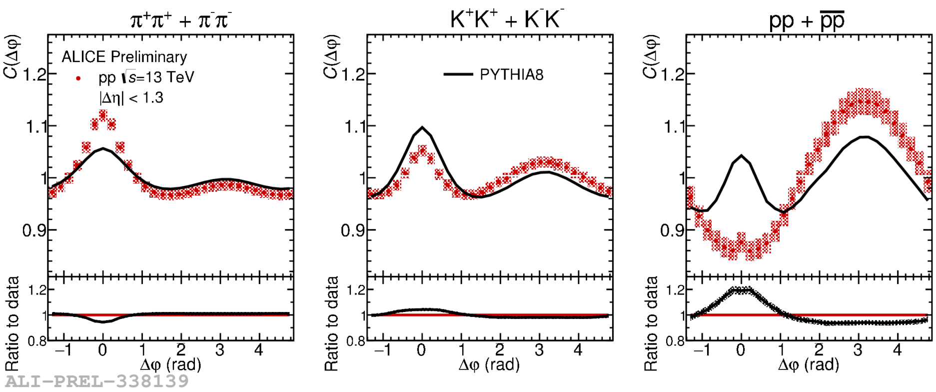

Figure 1.4: $\Delta\eta$ integrated projections of angular correlation functions for like-sign pairs of (left) pions, (center) kaons and (right) protons.

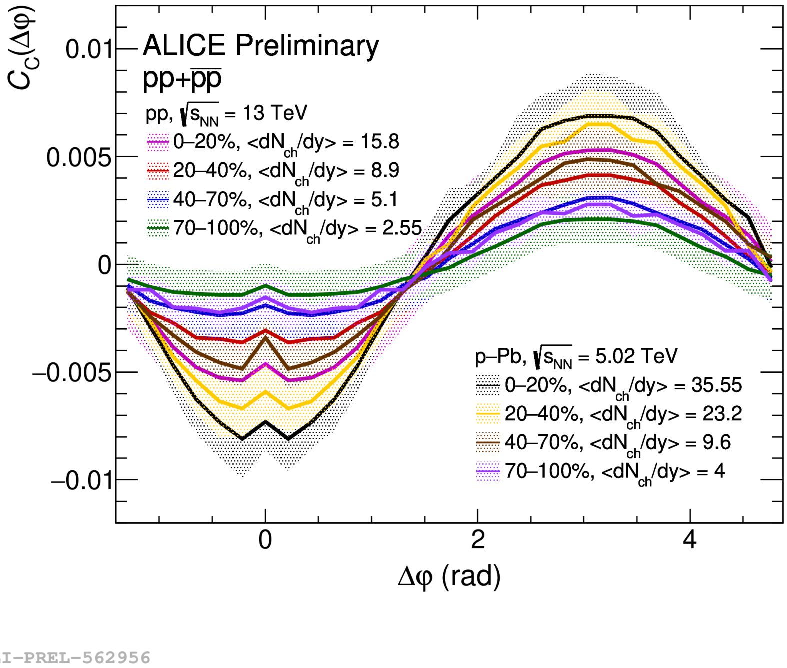

Figure 1.5: Comparison of the $\Delta y \Delta \varphi$ correlation functions between the pp and pPb collisions at $\sqrt{s_{NN}}$ = 13 TeV and $\sqrt{s_{NN}}$ = 5.02 TeV, respectively. The comparison is made for protons with like-sign overall multiplicity classes analyzed by using the rescaled two-particle cumulant definition.

A similar study was carried out in the ALICE experiment for the p–Pb system at energy $\sqrt{s_{\mathrm{NN}}}$ = 5.02 TeV and pp at energy $\sqrt{s_{\mathrm{NN}}}$ = 13 TeV in different multiplicity classes. A comparison of the $\Delta y \Delta \varphi$ correlation functions for pp + $\bar{p}\bar{p}$ pairs in the two systems has been made in the plot 1.5. This result proves once again that the anticorrelation that was observed is not dependent on the studied system and the effect is stronger for the lower multiplicity classes.

Because theoretical models used now cannot replicate the shape obtained from the experimental data, some modifications have been made to the simulation models. One of the changes to the PYTHIA model proposed in recent years adds two alterations to the fragmentation code [10]. The two modifications are as follows:

- ***"always baryon"*** - fragmentation of a single string always produces one baryon, which ensures good agreement with data, but does not impose any physical meaning,
- ***"one baryon"*** - it ensures the Pauli principle on baryons by producing at maximum a single baryon from each string.

Those code modifications enable PYTHIA to reproduce the anticorrelation for baryons, which can be seen in figure 1.6, which shows correlation functions C and azimuthal projections of the correlation functions for the studied baryon-baryon and baryon-antibaryon pairs using one-baryon modification to the fragmentation code. This paper suggests that producing two baryons or two antibaryons from the same string is highly unlikely.

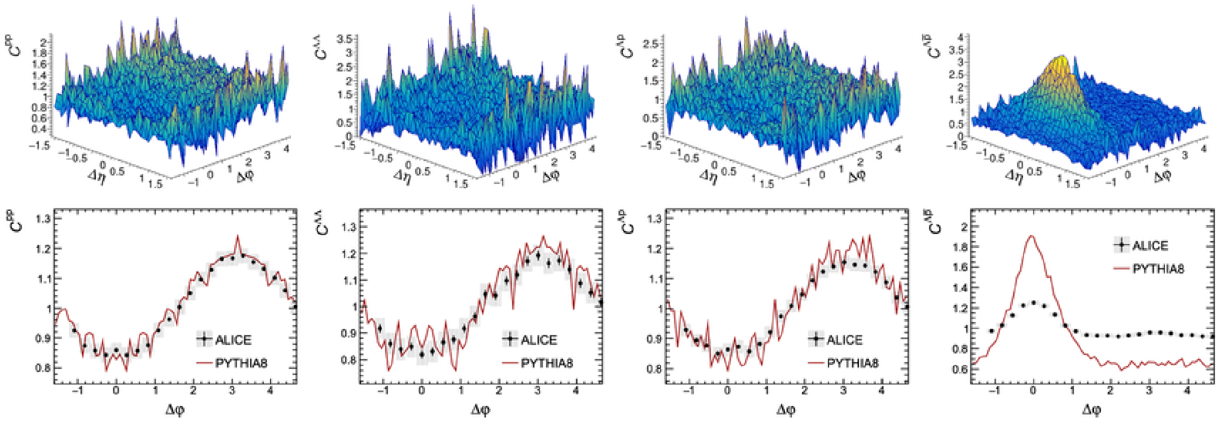

Figure 1.6: Correlation functions C (top row) for pp, $\Lambda\Lambda$, Λp and $\Lambda\bar{p}$ in pp PYTHIA8 collisions applying the **one-baryon** policy. Azimuthal projection (bottom row) of the correlation function C for pp, $\Lambda\Lambda$, Λp and $\Lambda\bar{p}$ compared to ALICE data [7, 10].

More physical mechanisms have been proposed by the authors in the [11]. They derived their modification from the popcorn model. As a result, the production of baryons near the gluon kinks was suppressed.

The answer to the question of the baryon anticorrelation remains open. Theoretical physicists working on that topic need new experimental input, especially from angular and femtoscopic correlation functions of different mesons. The analysis of Φ mesons is particularly interesting, by the fact that their mass is close to that of the proton, which is the lightest baryon. This study helps to answer the question of whether or not the obtained anticorrelation is a mass effect, which is the aim of this thesis. To perform this study I have used ALICE pp collisions at $\sqrt{s_{\rm NN}}$ = 13.6 TeV and the newest ALICE O^2 software. The details of this study will be described in the later chapters of this work.

Chapter 2

Experimental setup

2.1. CERN

CERN (Conseil Européen pour la Recherche Nucléaire) is one of the largest scientific centres on Earth. This international laboratory is located on the border between France and Switzerland near Geneva [12]. The main focus of the institute is particle physics research. Discoveries made at CERN allow pushing the boundaries of technology and advances the science developement by deepening our understanding of the universe.

At CERN, the existence of the *God Particle* – Higgs boson – was confirmed [13]. In addition, it was at CERN that Tim Berners-Lee invented the World Wide Web (WWW) [14], to more efficiently transfer data between scientists working at institutions around the world. Furthermore, research conducted at CERN has allowed significant development of PET (Positron-Emission-Tomography) medical imaging technology [15] and hadron therapy [16]. By bringing together scientists from all over the world, CERN allows us to better understand the world around us and pushes the frontiers of science forward.

2.2. LHC

LHC (Large Hadron Collider) is the world's largest and most powerful particle accelerator [17]. It is 26.6 km long and it's the largest machine built to this day [18]. It is a part of the system of accelerators, which is used to speed up the particles and ions (mainly protons and lead nuclei) to near the speed of light. The Large Hadron Collider is the final component of the accelerator complex at CERN, which is shown in figure 2.1.

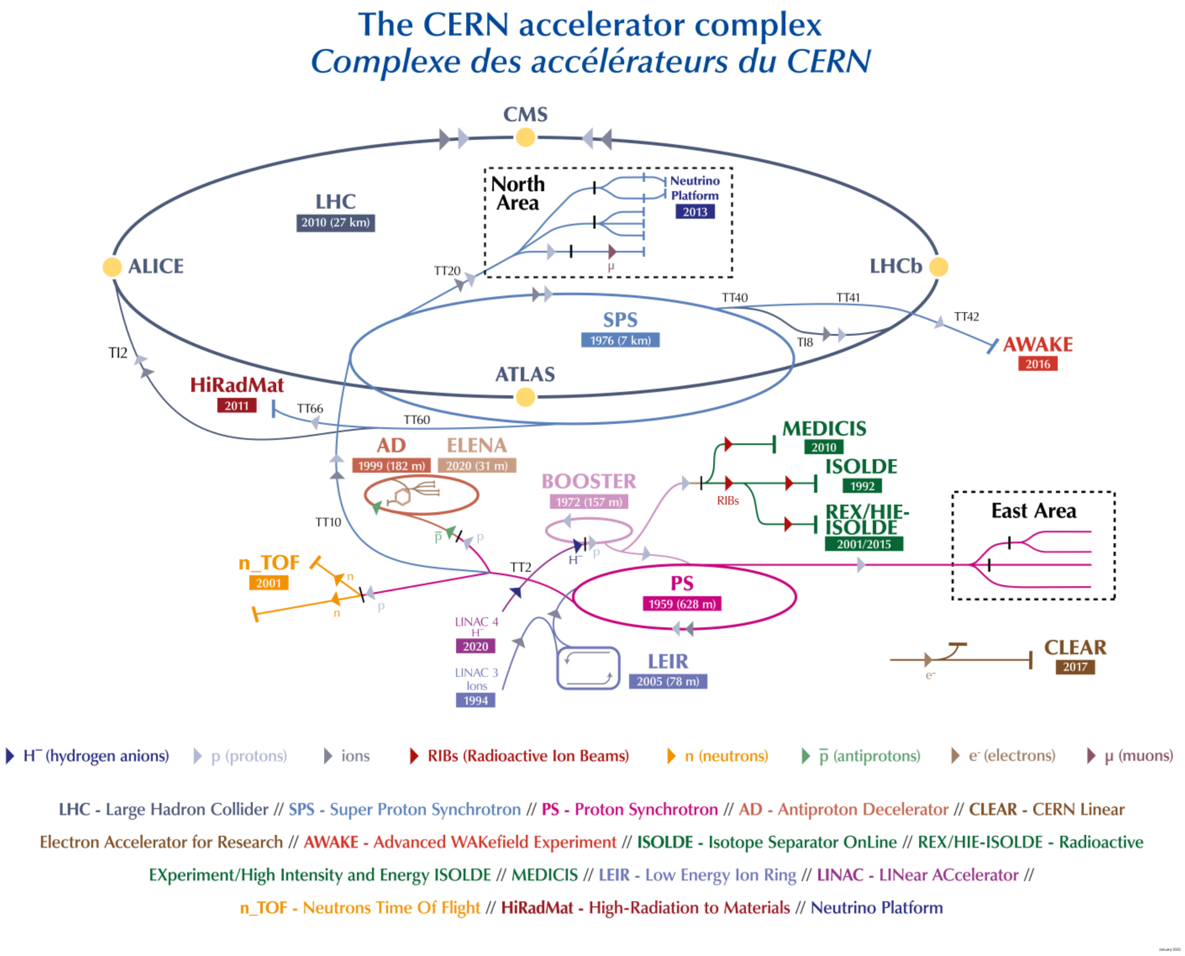

Figure 2.1: The CERN accelerator complex [19].

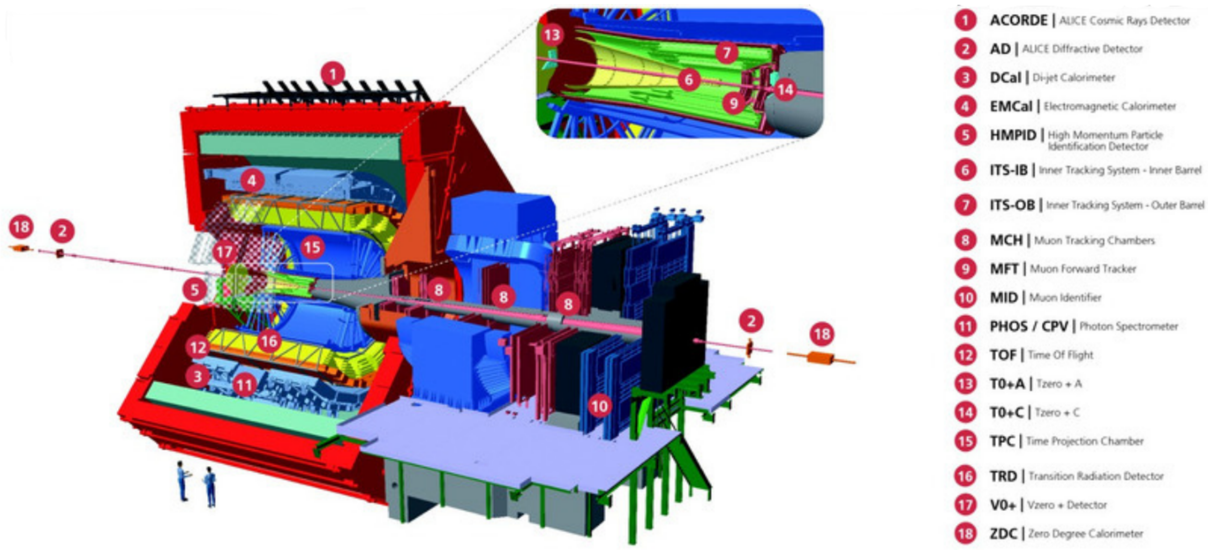

Figure 2.2: ALICE detector schematics for the Run 3 and Run 4 [24].

2.3. ALICE

One of the four experiments at the LHC is ALICE (A Large Ion Collider Experiment) [20]. The primary goal of the research conducted by the scientists working on the ALICE experiment is to understand the nature of quark-gluon plasma (QGP) [21]. It is postulated that this was the state of matter that existed directly after the Big Bang. In this condition, quarks and gluons – that make up the matter surrounding us everywhere – were in an unbound state.

During Long Shutdown 2 (2018-2022) ALICE experiment upgraded a lot of its detectors [22]. That was driven by the need to adapt to the new higher frequency of collisions and data collection. Those changes will also increase the efficiency of track reconstruction. In addition, a key goal was to achieve greater precision in the detection of short-lived particles [23]. In figure 2.2 ALICE detector schematics for the Run 3 and Run 4 are presented. During LS2 ALICE collaboration has upgraded the following components of the experiment:

- Time Projection Chamber *TPC*,
- Inner Tracking System *ITS*,
- Fast Interaction Trigger *FIT*,
- Muon Forward Tracker *MFT*,
- Readout system.

Scientists and students from the Faculty of Physics at Warsaw University of Technology are contributing to the development of the ALICE experiment by analyzing the data [25] and developing the subsystems of the ALICE detector [26]. The FIT detector is explained in greater detail in the section 2.4.3.

2.4. ALICE subdetectors

Detectors that are particularly crucial for this analysis are TPC, TOF, FIT and ITS. They are described in detail in sections 2.4.1 - 2.4.4.

2.4.1. Time Projection Chamber (TPC)

The Time Projection Chamber [27] measures charged particles traversing its volume. On the path of their flight studied particles are ionizing gas electrons. Those electrons then travel in a uniform electric field towards the end plates. The third coordinate can be calculated from the arrival time of drifted electrons. Time Projection Chamber is used in the ALICE experiment to identify particles and to reconstruct their trajectories.

TPC detector provides information on average energy loss over the distance of a charged particle $\langle \frac{dE}{dx} \rangle$. This information can be used as a form of particle identification since different types of particles follow different curves in this distribution. The theoretical values for those values for different species of particles are given by the semi-empirical Bethe-Bloch formula 2.1. One can try to identify a particle by calculating how far (in standard deviations) it is from the theoretical value.

$$-\left\langle \frac{dE}{dx} \right\rangle = Kz^2 \frac{Z}{A} \frac{1}{\beta^2} \left[\frac{1}{2} \ln \frac{2m_e c^2 \beta^2 \gamma^2 T_{max}}{I^2} - \beta^2 - \frac{\partial(\beta\gamma)}{2} \right] \tag{2.1}$$

2.4.2. Time-of-Flight detector (TOF)

The second detector that is important for particle identification is the TOF detector [28]. Its readout electronics were upgraded during the Long Shutdown 2 [29]. It is located about 3.7 m from the interaction point and constructed from the Multigap Resistive Plate Chamber (MRPC) strip detector units.

Using this device it is possible to measure the time of flight of the studied particle with an accuracy better than a tenth of a billionth of a second [30]. This information, combined with the particle trajectory measured by the TPC detector, allows a particle's velocity to be determined with unprecedented accuracy. From this, the mass of the particle can be determined.

2.4.3. FIT

The FIT (Fast Interaction Trigger) detector acts as an interaction trigger. Because of that, it is the most important detector used in the ALICE experiment. Without it working, data cannot be collected properly for the physics analysis. It consists of three sub-detectors: FT0, FV0, and FDD.

During Long Shutdown 2, the readout electronics were improved to allow continuous readout necessitated by the increased interaction rate for Run 3. The FIT detector after the upgrade delivers triggering which is required for successful data taking, but also luminosity and forward multiplicity measurements and fast timing used for TOF [29].

2.4.4. ITS

The ITS detector is capable of measuring the trajectory of charged particles and their momentum. It also allows the reconstruction of primary and secondary vertices. When a charged particle passes through the detector, it releases electrons by ionizing the material. Electrons can diffuse laterally, while vertical electrons are limited by potential barriers at the interfaces with underlying p-wells and p-type substrates. The signal-detecting elements are n-well diodes ($\approx$2 μm in diameter). Carriers that reach the diode's depletion volume induce a current signal at the pixel's front-end input.

There was a major improvement in the ITS detector during Long Shutdown 2. The main goal was to improve the reconstruction of the primary vertex as well as decay vertices coming from hadrons with heavy flavor and to improve the detection performance of particles with low p_T [31].

Chapter 3

Software environment

3.1. O^2 framework

Due to the huge changes introduced during Long Shutdown 2 (LS2), a major rewrite of the software used was necessary. New ALICE O^2 software enables reconstruction, calibration, and simulation of the ALICE data [32]. Together with the new software, a common data model and many algorithms such as global tracking have been introduced.

Apache Arrow [33] is a language-agnostic and open-source columnar in-memory data representation format, that is designed for efficient and high-performance analytics. New ALICE O^2 software is using Apache Arrow tables, as a way to organize and store data in a columnar format that is optimized for modern hardware architectures, such as CPUs and GPUs. Designed to support zero-copy sharing for lightning-fast data access. Due to the language-agnostic approach it enables cross-language compatibility between different programming languages, such as C++, Python, and more. The columnar data layout comes with several advantages, including better compression, improved cache utilization, and the ability to perform vectorized operations on data.

With the new ALICE O^2 software came a new way to record data using flat arrays. Each row of the array represents a different entity (such as collisions or particles), and each column represents physical measurements. The data collected during Run 3 and Run 4 are written in the form of the structure of arrays. The data is collected continuously, using time markers for subsequent segmentation into segments called Time Frames (TFs).

New ALICE software used for the data analysis uses so-called declarative programming. It is encoded in the ALICE O^2 Data Processing Layer (DPL). The declarative programming paradigm differs from the imperative one in the sense that it expresses the logic of computation by describing what the program should achieve and not how it should do it.

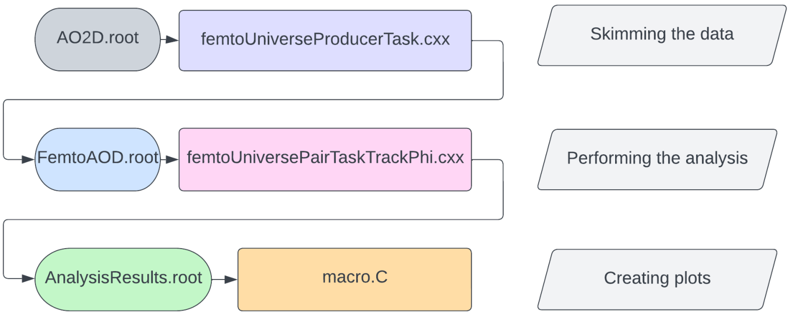

Figure 3.1: The simplified code flow for the p–Φ analysis.

3.2. FemtoWorld and FemtoUniverse modules in the O^2 software

The ALICE collaboration is slowly moving its analyses to new O^2 software. As a result, many packages have already been developed to enable various types of physical analyses. Packages dedicated to analyses carried out by the Warsaw University of Technology group are called FemtoWorld and FemtoUniverse. The simplified code flow for the p–Φ analysis is presented in the 3.1 figure.

As a bachelor thesis project, in June of 2022, I started developing a toy package for physical analyses performed at WUT, called FemtoWorld. I have been able to provide very preliminary angular and femtoscopic correlation function results and QA plots for studied particles. The developed code served its purpose and, in addition to the initial results, allowed for a better familiarity with the complex and constantly evolving software. The results I received while writing my engineering thesis were far from ideal. I had a very low statistic in the p–Φ correlations, and no physical result could be observed.

The group working on the FemtoWorld package continued to grow, and in the summer of 2023 with the knowledge I gained, I created a new analysis package – FemtoUniverse. The new code is more modular and is performing much better than the previous one. This is already allowing physical results for many analyses both in experimental and Monte Carlo data.

Generation of derived data

The first important step for the analysis using the FemtoUniverse package is the generation of the derived data. From the ALICE detector system, we can get signals that require additional processing and complex reconstruction. From the obtained data points we are able to derive physical observables of a particle, such as charge, momentum and mass. However, not all observables stored in general-purpose data are necessary for this analysis. Performing analyses on such enormous datasets would waste computational resources. To avoid that, we perform data skimming. By running the *Producer* task we strip the data from the unnecessary parts (unwanted variables, particles or collisions rejected at this initial step etc.). Using the *Producer* task we are also able to reconstruct the particles such as Φ mesons, V0s or D mesons.

3.3. Hyperloop

Hyperloop enables its users to run their analysis on a given dataset. Locally one can test the performance of an analysis on a few GB of data, whereas using the train system it is possible to run on a few TB of data to up to a few hundred TB. To achieve that the code is being run on the GRID computing network, which will be described in detail in the 3.4 section.

The new Hyperloop train system emerged with the upgrade of the software. It is presented in the form of a website, which GUI is based on the React.js library. It uses a PostgreSQL database for storage and a Java-based model for bookkeeping of wagons and datasets [34].

3.4. GRID

The Worldwide LHC Computing Grid (WLCG) is a computing infrastructure designed to handle massive amounts of data produced by the LHC, it provides means to store, process and analyze the LHC data. It draws inspiration from the electric grid, in which different power producers are interconnected to provide end users with standardized voltage and frequency. Similarly, GRID connects scattered computer resources, data services, and processor farms over the Internet, providing standard protocols for program execution and output download [35]. It is developed by international collaboration in over 170 sites in 42 countries. Each day, it allows about 2 mln tasks to run [36]. Figure 3.2 depicts Tier-1 and Tier-2 sites of Worldwide LHC Computing GRID and figure 3.3 shows transfer throughput of GRID network.

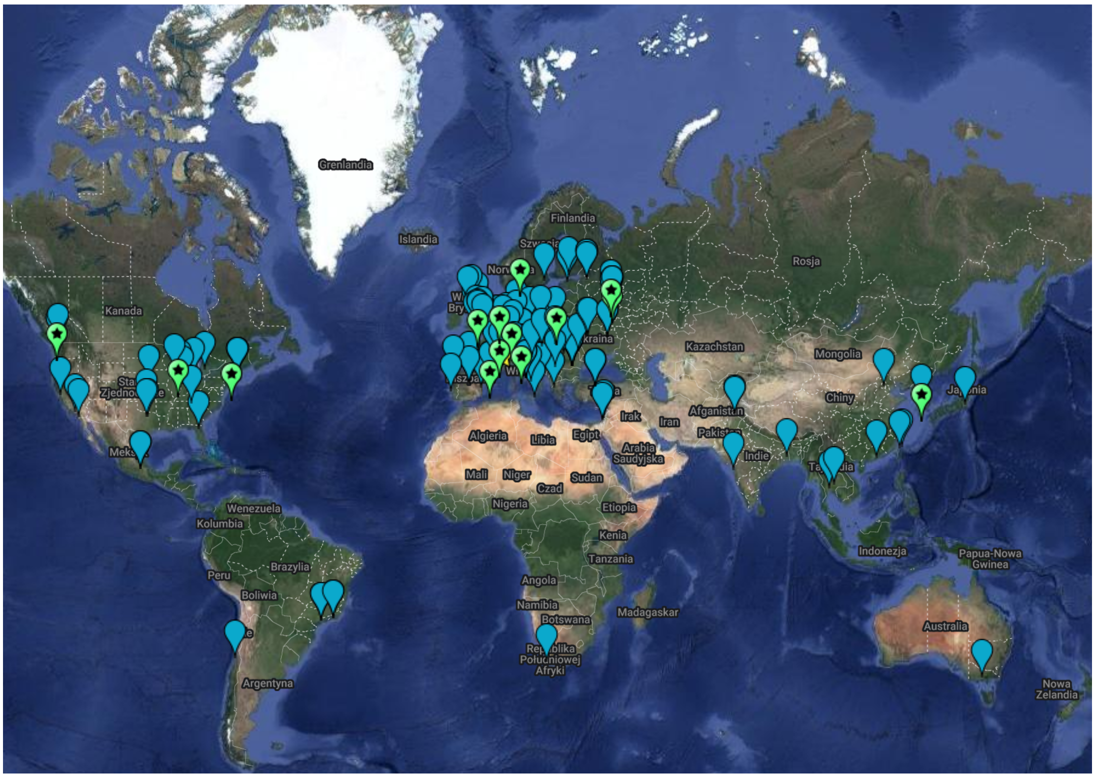

Figure 3.2: Worldwide LHC Computing GRID. Tier-1 sites are marked in green and Tier-2 sites are highlighted in blue [37].

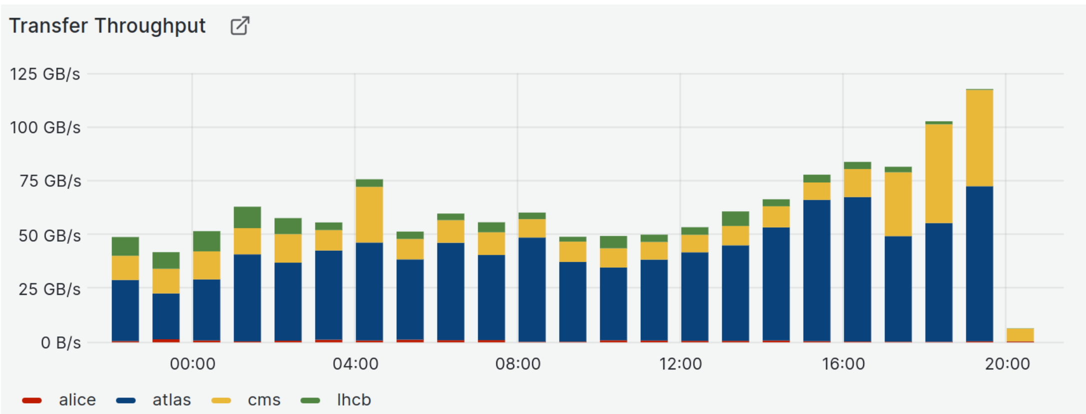

Figure 3.3: WLCG 24 hours transfer throughput on 27.12.2023 [37].

Chapter 4

Scientific tool – angular correlations

Hadronization mechanisms can be studied using angular correlation functions. This powerful tool is sensitive to a number of various physical effects. By comparing the angular correlation functions obtained from the data with those derived from the Monte Carlo simulation models, one can assess the accuracy of the models used to reproduce the hadron production. As a tool, angular correlation functions can be used in both heavy ion and proton collisions. These correlations are conventionally represented in the $\Delta\eta\Delta\varphi$ variables, where $\Delta\eta$ is the difference in pseudorapidity, while $\Delta\varphi$ is the difference in azimuthal angle between the two particles. Experimentally, we can define the angular correlation function according to the equation 4.1.

$$C(\Delta\eta, \Delta\varphi) = \frac{N^{\text{mixed pairs}}}{N^{\text{signal pairs}}} \frac{S(\Delta\eta, \Delta\varphi)}{B(\Delta\eta, \Delta\varphi)}, \tag{4.1}$$

where $\Delta\eta = \eta_1 - \eta_2$ is a difference in the pseudorapidity and $\Delta\varphi = \varphi_1 - \varphi_2$ is a difference in the azimuthal angle. $S(\Delta\eta, \Delta\varphi)$ is the signal distribution, which is obtained by correlating particles coming from the same event. Because of the inefficiencies of the physical detectors, it is necessary to calculate the background distribution $B(\Delta\eta, \Delta\varphi)$, which is formed by calculating the difference in pseudorapidity and azimuthal angle of particles from different events. To do that process called event mixing is used. In the process of event mixing, particles from different collisions are correlated with each other. Figure 4.1 shows example distributions of signal distribution, background distribution and angular correlations function.

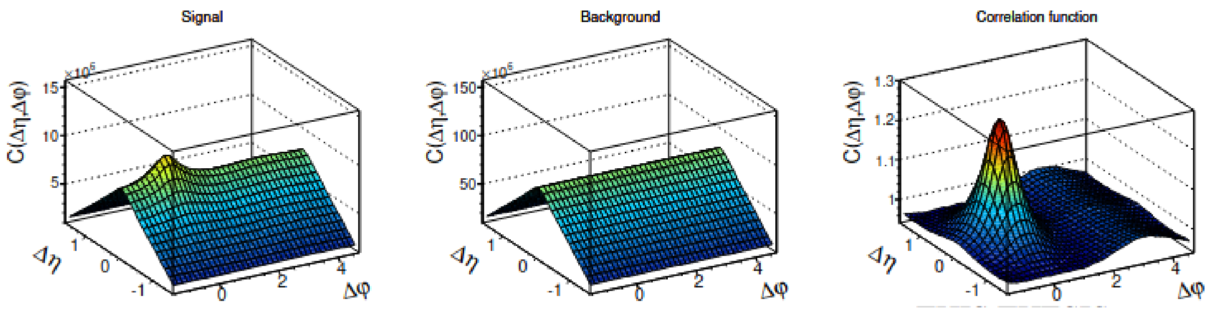

Figure 4.1: Construction of the $\Delta\eta\Delta\varphi$ correlation function. Signal distribution (left), background distribution (middle), and correlation function (right) [38].

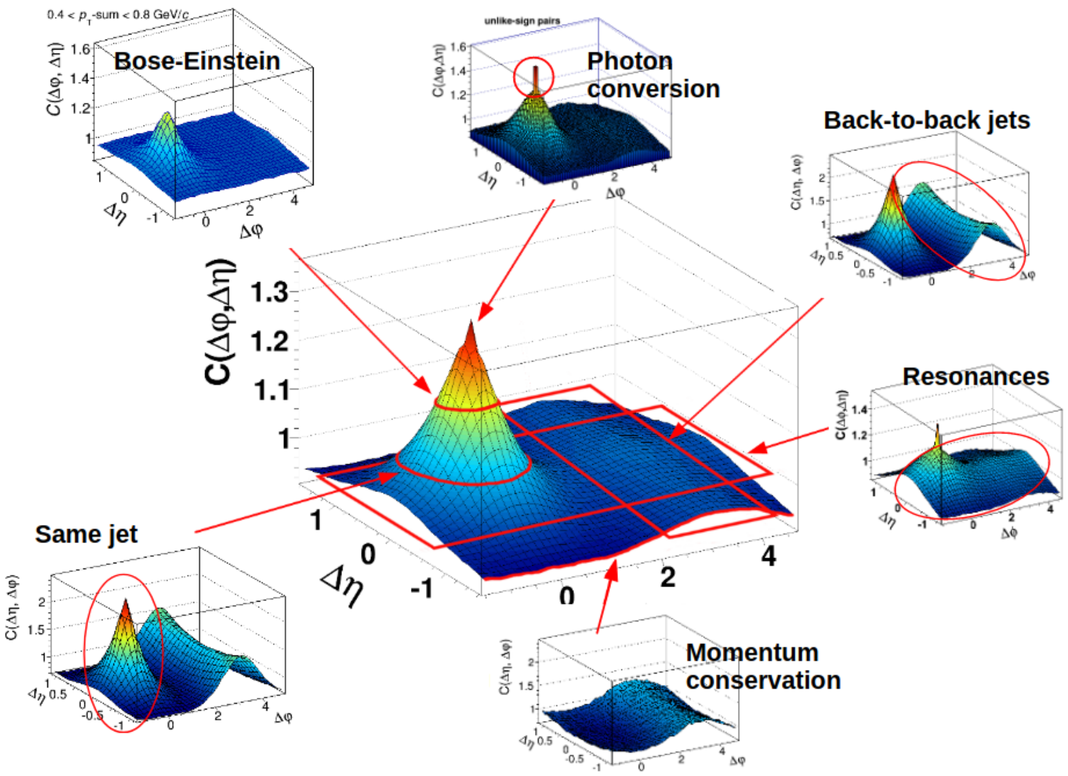

Figure 4.2: Schematic of the angular correlation function $C(\Delta\eta, \Delta\varphi)$ showing contributions from various correlation sources [39].

Typical distributions of angular correlations have a peak around the (0,0) point and a ridge for $\Delta\varphi = \pi$. The effects that comprise the studied characteristics include resonance decays, energy and momentum conservations, and Coulomb interactions. Exemplary components of angular correlations are shown in figure 4.2. Using various constraints on the observable of the studied particles, it is possible to enhance the individual components. For instance, particles with high momentum should be studied for contributions coming from jets. By rejecting low momentum particles from the analysis, it is possible to increase the contribution coming from jets' interactions. In this case, we observe an increase in the peak near the (0,0) point, because the jet produces a lot of particles close together in the $\Delta\eta\Delta\varphi$ space. On the other hand, to conserve momentum so-called back-to-back jets are formed. By their presence, we observe the previously mentioned ridge because the difference in azimuthal angle between the particles from these two jets is equal to π.

Chapter 5

Data analysis

5.1. Data sample

The analysis was carried out on the data presented in the 5.1 table. A minimum bias trigger was used. Figure 5.1 presents the multiplicity distribution for the studied dataset. The multiplicity distribution indicates how many MIPs (minimum ionizing particles) are collected by the detector.

5.2. Particle selection criteria

5.2.1. Proton selection criteria

Table 5.2 provides selection criteria for protons. A low momentum p_{T} cutoff is used to minimize the number of protons from primary particle interactions with the detector material. Selection at high p_{T} allows for increased purity of selected particles. Figures 5.2 – 5.4 show p_{T}, η, φ spectra for protons, while 5.6 and 5.7 depict $n_{\sigma,\mathrm{TPCp}}$ vs p and $n_{\sigma,\mathrm{TOFp}}$ vs p distributions respectively.

5.2.2. Φ candidate selection criteria

Φ mesons decay via strong interaction after ~$1.5 \cdot 10^{-22}$ s [40]. The most common decay channel is K^+K^- ($BR_{\Phi\to K^+K^-} = (49.1 \pm 0.5)\%$ [41]). To properly reconstruct Φ meson it is important to correctly identify its daughters. To achieve that PID selection criteria were applied for the n_σ^{TPC} and n_σ^{TOF} values. Those kaons had also basic p_{T}, η and φ and global track selection criteria set. All of the selections for kaons were described in the 5.3 and 5.4 tables.

Table 5.1: Datasets used for this analysis.

	Description	Dataset	Run range
ALICE data	appas4 of LHC22o - 13.6 TeV	LHC22o_pass4_minBias_small	526641
		LHC22o_pass4_minBias	526641, 526964, 527041, 527057, 527109, 527240, 527850, 527871, 527895, 527899, 528292, 528461, 528531
MC data	pp, 13.6 TeV - LF-resonance injected	LHC23f3b	302001

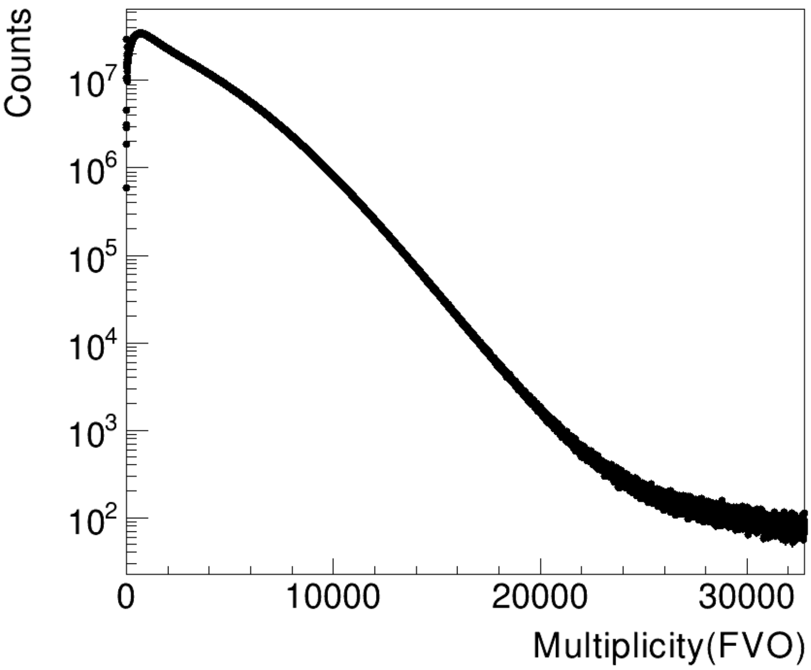

Figure 5.1: Multiplicity distribution, ALICE pp collisions at $\sqrt{s}$ = 13.6 TeV.

In the next step, an invariant mass value was obtained for the $K^{+}K^{-}$ pair. Later, the Φ meson observables were reconstructed using Lorentz vectors. The selection criteria for the Φ meson candidate can be seen in the 5.5 table.

Table 5.2: Proton selection criteria.

Selection criteria	**Value**
Transverse momentum	$p_{\mathrm{T}} \in (0.1; 2.5)$ GeV
Pseudorapidity	$\lvert\eta\rvert < 0.8$
IsGlobalTrack	True
Particle Identification	$\lvert n_{\sigma,\mathrm{TPC}}\rvert < 3.0$ for $p < 0.3$ GeV/c
	$\lvert n_{\sigma,\mathrm{TPC}}\rvert < 3.0$ and $\lvert n_{\sigma,\mathrm{TOF}}\rvert < 3.0$ for $p < 0.3$ GeV/c

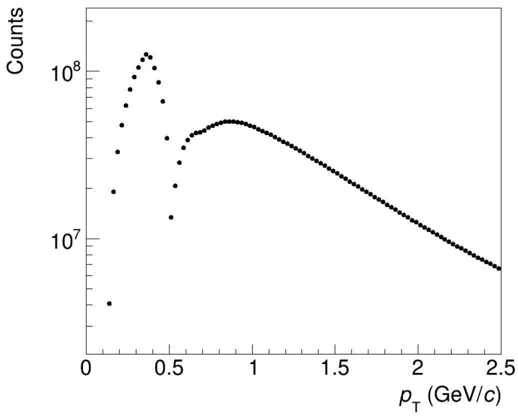

Figure 5.2: p_T spectra for protons, ALICE pp collisions at $\sqrt{s_{NN}} = 13.6$ TeV.

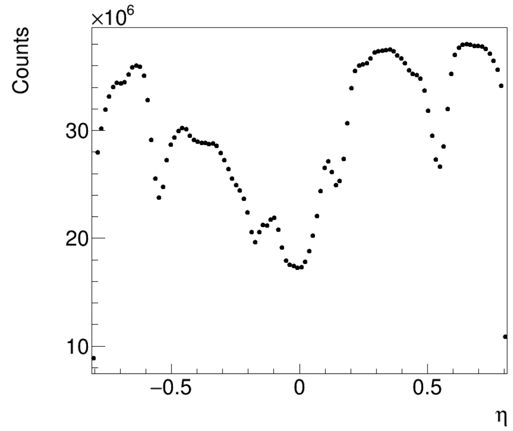

Figure 5.3: η spectra for protons, ALICE pp collisions at $\sqrt{s_{NN}} = 13.6$ TeV.

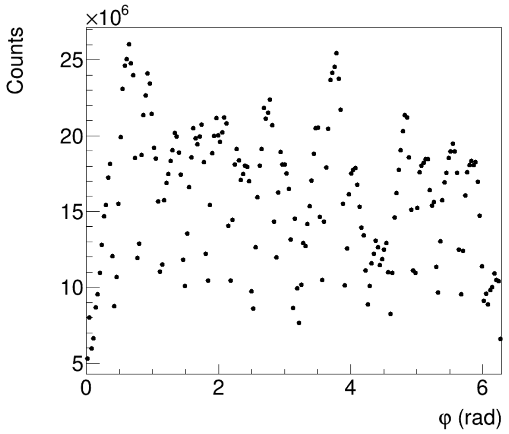

Figure 5.4: φ distribution for protons, ALICE pp collisions at $\sqrt{s_{NN}} = 13.6$ TeV.

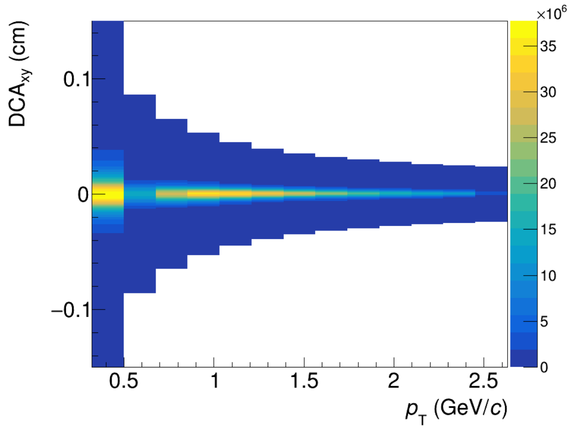

Figure 5.5: DCA_{xy} for protons, ALICE pp collisions at $\sqrt{s_{NN}} = 13.6$ TeV.

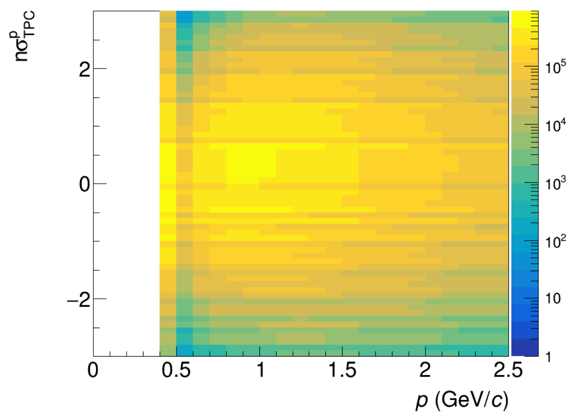

Figure 5.6: $n_{\sigma,\mathrm{TPCp}}$ for protons, ALICE pp collisions at $\sqrt{s_{NN}} = 13.6$ TeV.

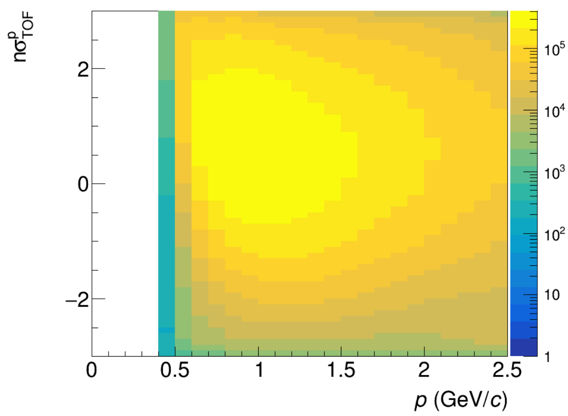

Figure 5.7: $n_{\sigma,\mathrm{TOFp}}$ for protons, ALICE pp collisions at $\sqrt{s_{NN}} = 13.6$ TeV.

Table 5.3: Kaon selection criteria.

Selection criteria	Value
Transverse momentum (GeV/c)	$p_T \in (0.14; 4.0)$
Pseudorapidity	$\|\eta\| < 0.8$
IsGlobalTrack	True
Particle Identification	$\|n_{\sigma,TPC}\| < 3.0$ for $p < 0.3$ GeV/c
	$\|n_{\sigma,TPC}\| < 2.0$ for $p \in (0.30; 0.45)$ GeV/c
	$\|n_{\sigma,TPC}\| < 1.0$ for $p \in (0.45; 0.55)$ GeV/c
	$\|n_{\sigma,TPC}\| < 3.0$ and $\|n_{\sigma,TOF}\| < 3.0$ for $p \in (0.55; 1.50)$ GeV/c
	$\|n_{\sigma,TPC}\| < 3.0$ and $\|n_{\sigma,TOF}\| < 2.0$ for $p > 1.5$ GeV/c

Table 5.4: Global track selection criteria.

Selection criteria	Value
min number of crossed rows TPC	70
min ratio of crossed rows over findable clusters TPC	0.8
max χ^2 per cluster TPC	4.0
max χ^2 per cluster ITS	36.0
require TPC refit	true
require ITS refit	true
max DCA to vertex z (cm)	2.0
max DCA to vertex xy (cm)	0.0105 * 0.035 / $p_T^{1.1}$
cluster requirement ITS	Run 2 (Run 3): at least one hit in SPD
p_T range (GeV/c)	0.1 - 1e10
η range	-0.8 - 0.8

Table 5.5: Φ meson selection criteria.

Selection criteria	Value
Transverse momentum	$p_T \in (0.3; 4.3)$ GeV
Pseudorapidity	$\|\eta\| < 0.8$
Invariant mass	$m_{inv} \in (1.011; 1.027)$ $\frac{\text{GeV}}{\text{c}^2}$

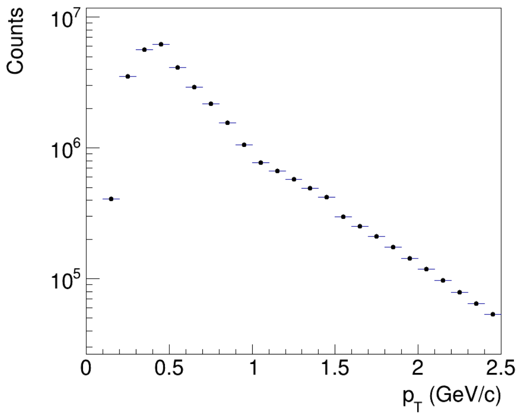

Figure 5.8: p_T spectra for K$^+$, ALICE pp collisions at $\sqrt{s_{NN}} = 13.6$ TeV.

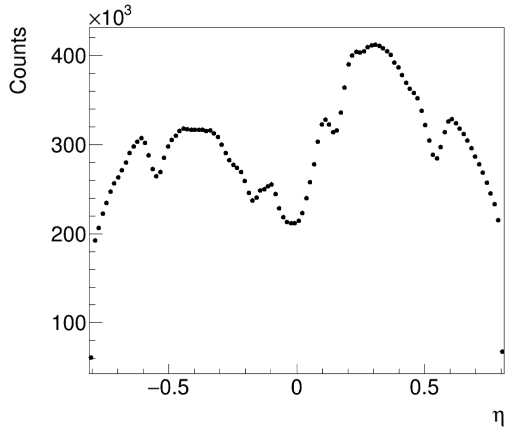

Figure 5.9: η spectra for K$^+$, ALICE pp collisions at $\sqrt{s_{NN}} = 13.6$ TeV.

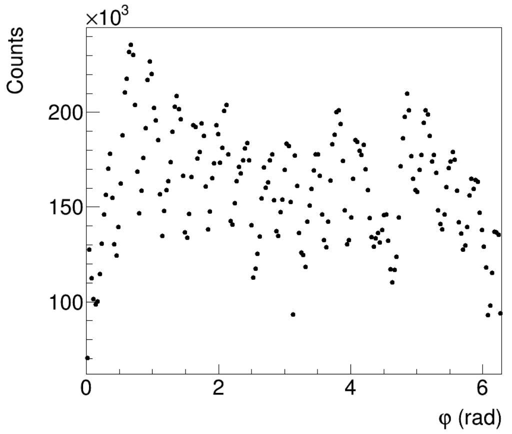

Figure 5.10: φ distribution for K$^+$, ALICE pp collisions at $\sqrt{s_{NN}} = 13.6$ TeV.

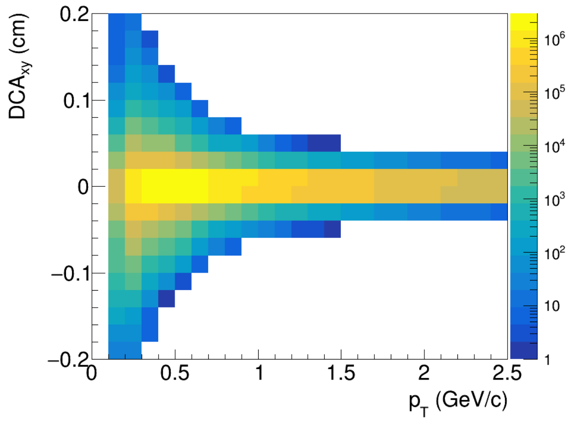

Figure 5.11: DCA$_{xy}$ for K$^+$, ALICE pp collisions at $\sqrt{s_{NN}} = 13.6$ TeV.

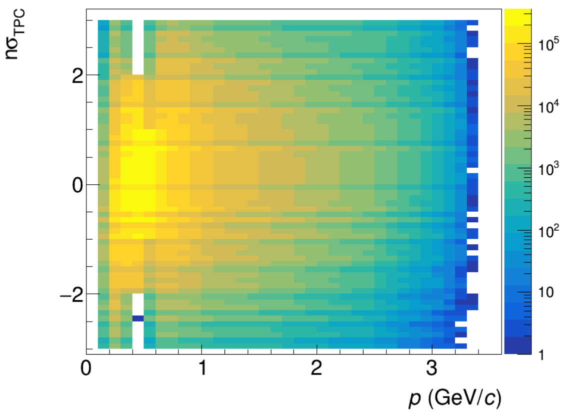

Figure 5.12: $n_{\sigma,\mathrm{TPCK}}$ for K$^+$, ALICE pp collisions at $\sqrt{s_{NN}} = 13.6$ TeV.

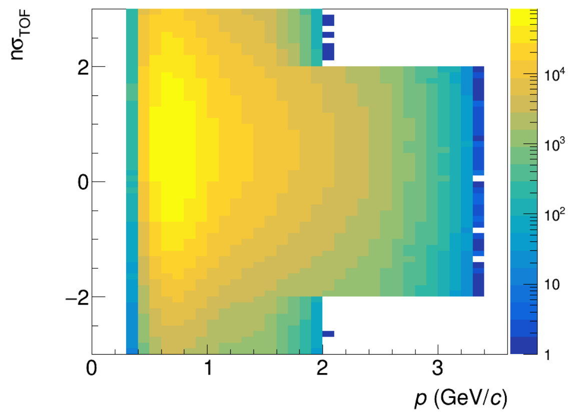

Figure 5.13: $n_{\sigma,\mathrm{TOFK}}$ for K$^+$, ALICE pp collisions at $\sqrt{s_{NN}} = 13.6$ TeV.

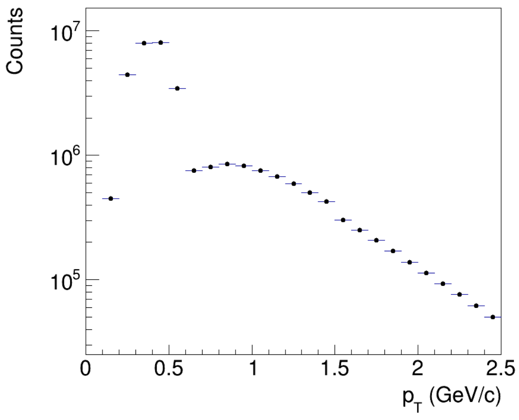

Figure 5.14: p_T spectra for K^-, ALICE pp collisions at $\sqrt{s_{NN}} = 13.6\,\text{TeV}$.

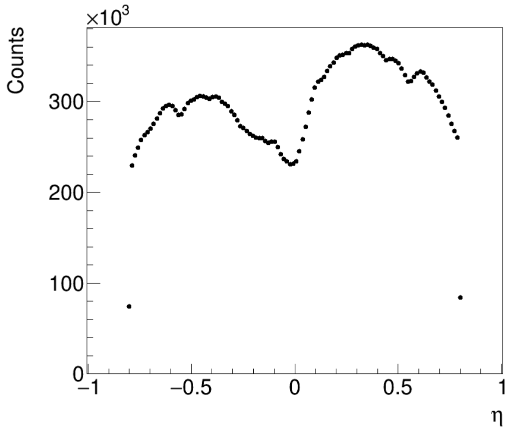

Figure 5.15: η spectra for K^-, ALICE pp collisions at $\sqrt{s_{NN}} = 13.6\,\text{TeV}$.

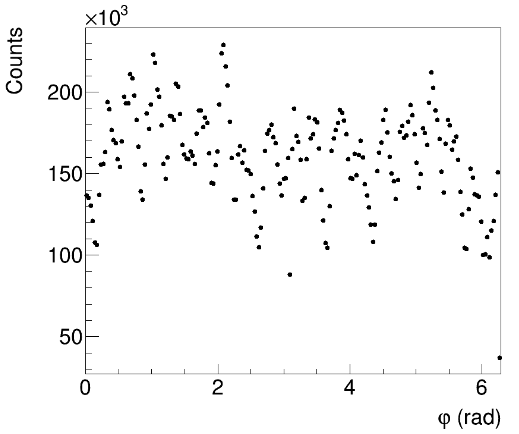

Figure 5.16: φ distribution for K^-, ALICE pp collisions at $\sqrt{s_{NN}} = 13.6\,\text{TeV}$.

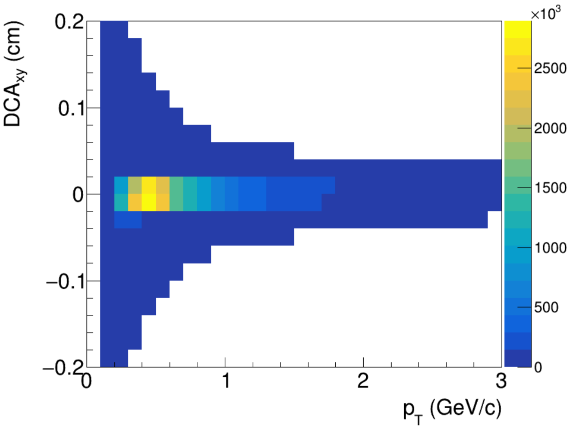

Figure 5.17: DCA_{xy} for K^-, ALICE pp collisions at $\sqrt{s_{NN}} = 13.6\,\text{TeV}$.

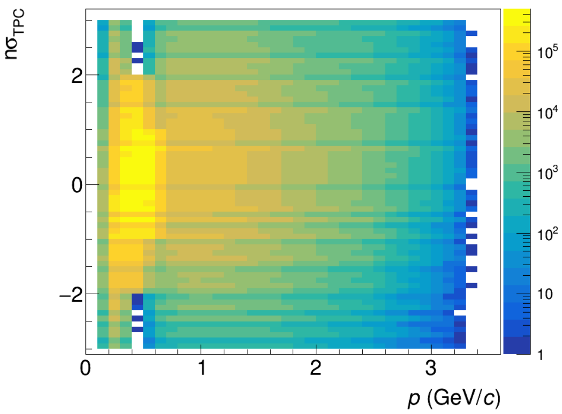

Figure 5.18: $n_{\sigma,\text{TPCK}}$ for K^-, ALICE pp collisions at $\sqrt{s_{NN}} = 13.6\,\text{TeV}$.

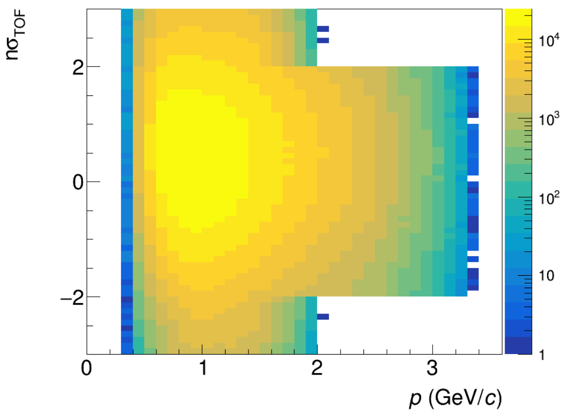

Figure 5.19: $n_{\sigma,\text{TOFK}}$ for K^-, ALICE pp collisions at $\sqrt{s_{NN}} = 13.6\,\text{TeV}$.

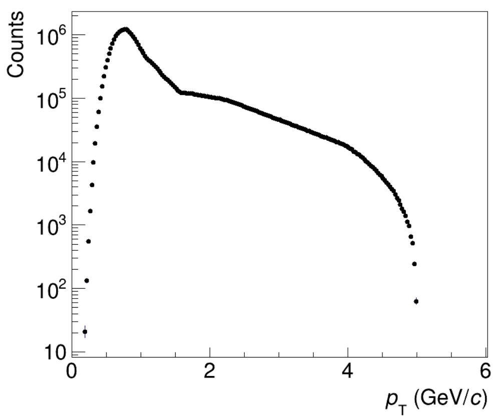

Figure 5.20: p_T spectra for Φ meson candidates, ALICE pp collisions at $\sqrt{s_{NN}}$ = 13.6 TeV.

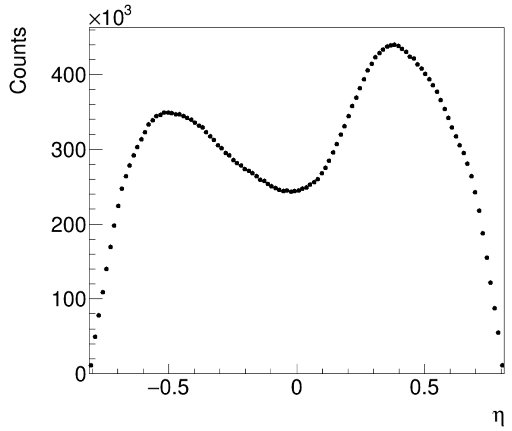

Figure 5.21: η spectra for Φ meson candidates, ALICE pp collisions at $\sqrt{s_{NN}}$ = 13.6 TeV.

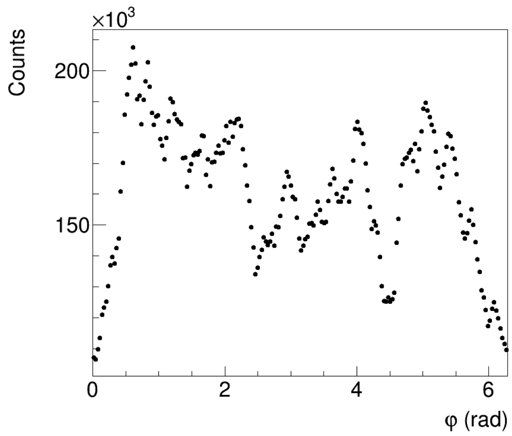

Figure 5.22: φ distribution for Φ meson candidates, ALICE pp collisions at $\sqrt{s_{NN}}$ = 13.6 TeV.

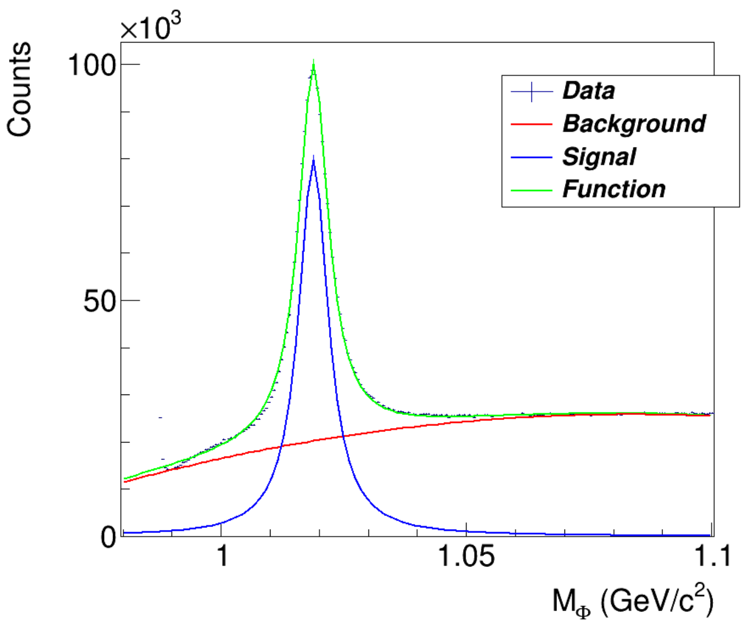

Figure 5.23: Invariant mass distribution for Φ meson candidates, ALICE pp collisions at $\sqrt{s_{NN}}$ = 13.6 TeV.

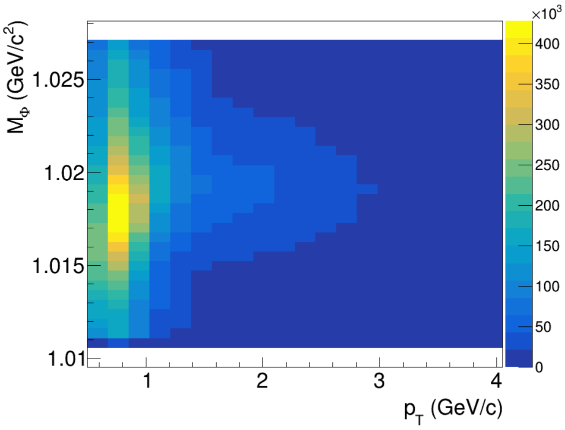

Figure 5.24: Invariant mass vs p_T distribution for Φ meson candidates with the invariant mass selection applied, ALICE pp collisions at $\sqrt{s_{NN}} = 13.6$ TeV.

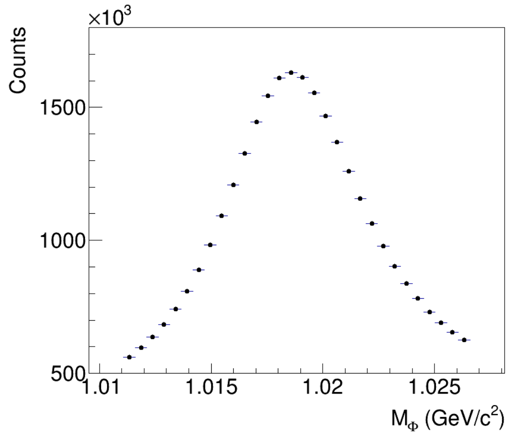

Figure 5.25: Invariant mass distribution for Φ meson candidates after selection, ALICE pp collisions at $\sqrt{s_{NN}} = 13.6$ TeV.

Calculating purity helps to identify the effectiveness of the selection criteria in separating the desired signal from unrelated background contributions. To obtain that, signal and background functions are fitted to the invariant mass distribution, which is shown in 5.23. In this analysis as a signal function lorentz peak is assumed, whereas for the background distribution second-degree polynomial was chosen. The purity in the chosen invariant mass range was estimated using the formula:

$$\text{Purity} = \frac{S}{S+B} \cdot 100\% = 65.33\%,$$

where S is the integral over the signal function in the limits shown in the table 5.5, while B is the integral over the background function in the same limits. Figure 5.24 shows the invariant mass vs p_T distribution after applying the invariant mass selection, while figure 5.25 depicts the invariant mass distribution for Φ mesons after applying the invariant mass selection.

5.3. Two track selection criteria

When reconstructing particles, it happens that traces left by one particle in detectors are interpreted as traces of two. At times, it also occurs that two particles are reconstructed as one. These effects are called splitting and merging effects, respectively. One of the most commonly used two-particle selection criteria to minimize those effects is $\Delta\eta\Delta\varphi^*$. Carrying out this selection is based on calculating the difference in the pseudorapidity $\Delta\eta$ and the difference in the azimuthal angle $\Delta\varphi^*$ calculated at a certain distance from the interaction point. In the case of this particular analysis, the radius from the interaction point was set to 0.8 m. To calculate $\Delta\varphi^*$ one uses the following formula:

$$\Delta\varphi^* = \varphi_1 - \varphi_2 + \arcsin\left(\frac{0.3 z_1 \cdot 0.1 B \cdot 0.01\,\text{rad}}{2 p_{T1}}\right) - \arcsin\left(\frac{0.3 z_2 \cdot 0.1 B \cdot 0.01\,\text{rad}}{2 p_{T2}}\right),$$

where φ is the azimuthal angle, B is the magnetic field, z is the particle charge, and p_{T} is the particle transverse momentum. The selection criteria used in this analysis has the following form: $|\Delta\eta| < 0.004 \wedge |\Delta\varphi^{*}| < 0.015$. The figures used for monitoring this selection are presented in the appendix. During the writing of this thesis, $\Delta\eta\Delta\varphi^{*}$ graphs were constructed as the sum of pairs derived from the same events and mixed events. In a later stage of the work, it is planned to divide the graphs of the plot obtained from correlating pairs originating from the same events by plot derived from pairs from mixed events.

Chapter 6

Results

In this section, the results obtained for the analysis of p–Φ angular correlations for both data (section 6.1) and MC data (section 6.3) are collected. In addition, I conducted angular correlation studies for p–p and the results for the data (section 6.2) are also included in this chapter. In addition, as a benchmark, I performed $\pi^+ - \pi^+$ angular correlation and the results can be found in the appendix.

6.1. Data results for the p–Φ angular correlations

Figures 6.1 - 6.1 represent signal and background distributions and figure 6.3 shows angular correlation function for p–Φ correlations measured using the pp collisions at $\sqrt{s_{\mathrm{NN}}} = 13.6\,\mathrm{TeV}$. Shown in the 6.4-6.9 figures are projections on the $\Delta\eta$ and $\Delta\varphi$ axes of the signal distribution, background distribution and angular correlation function.

6.2. Data results for the p–p angular correlations

Figures 6.10 - 6.10 represent signal and background distributions and figure 6.12 shows angular correlation function for p–p correlations measured using the pp collisions at $\sqrt{s_{\mathrm{NN}}} = 13.6\,\mathrm{TeV}$. Shown in the 6.13-6.18 figures are projections on the $\Delta\eta$ and $\Delta\varphi$ axes of the signal distribution, background distribution and angular correlation function.

6.3. MC data results for the p–Φ angular correlations

Figures 6.19 and 6.20 show signal and background distributions for the p–Φ correlation respectively, whereas 6.21 depict angular correlation function for p–Φ correlation. The plots have been obtained using the LHC23f4b2 Monte Carlo dataset, anchored to the LHC23o ALICE p–collision data. Figures 6.22 - 6.27 present projections on the $\Delta\eta$ and $\Delta\varphi$ axes of the signal distribution, background distribution and angular correlation function.

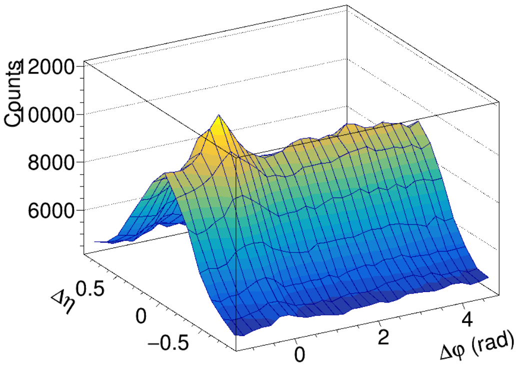

Figure 6.1: Signal distribution for p–Φ correlation, ALICE pp collisions at $\sqrt{s_{\mathrm{NN}}}$ = 13.6 TeV.

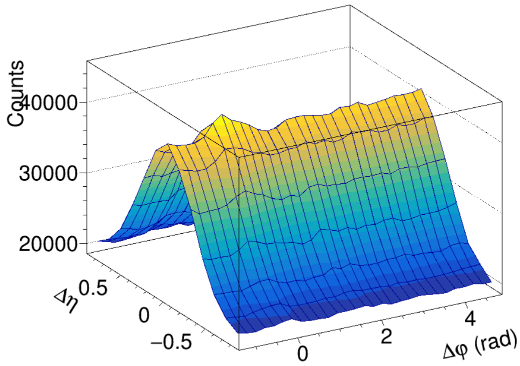

Figure 6.2: Background distribution for p–Φ correlation, ALICE pp collisions at $\sqrt{s_{\mathrm{NN}}}$ = 13.6 TeV.

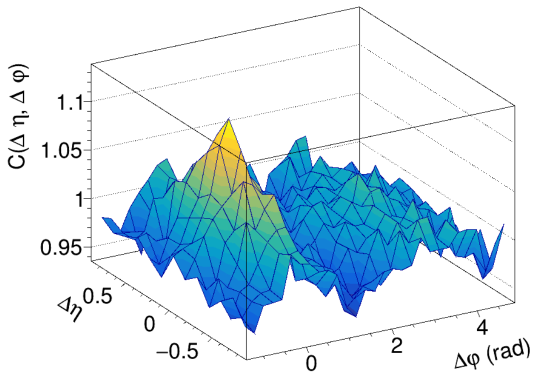

Figure 6.3: Angular correlation function for p–Φ correlation, ALICE pp collisions at $\sqrt{s_{\mathrm{NN}}}$ = 13.6 TeV.

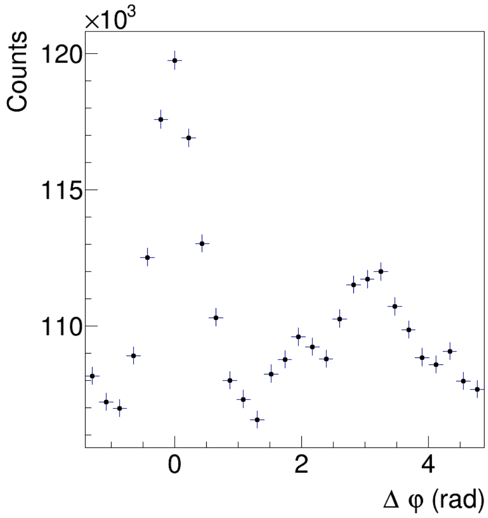

Figure 6.4: $\Delta\varphi$ projection of signal distribution for p–Φ correlation, ALICE pp collisions at $\sqrt{s_{\mathrm{NN}}}$ = 13.6 TeV.

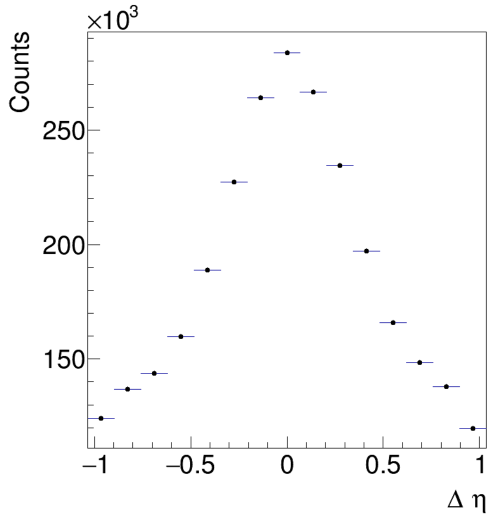

Figure 6.5: $\Delta\eta$ projection of signal distribution for p–Φ correlation, ALICE pp collisions at $\sqrt{s_{\mathrm{NN}}}$ = 13.6 TeV.

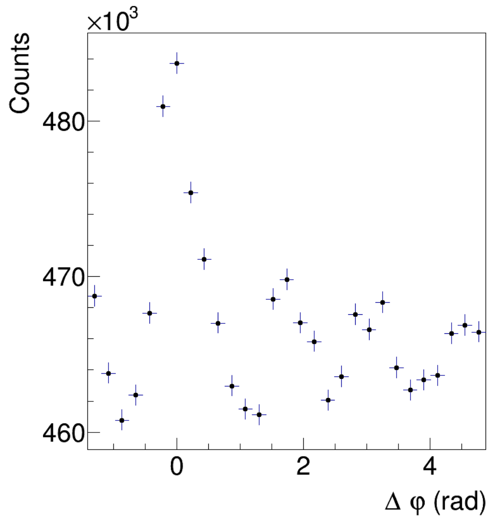

Figure 6.6: $\Delta\varphi$ projection of background distribution for p–Φ correlation, ALICE pp collisions at $\sqrt{s_{NN}}$ = 13.6 TeV.

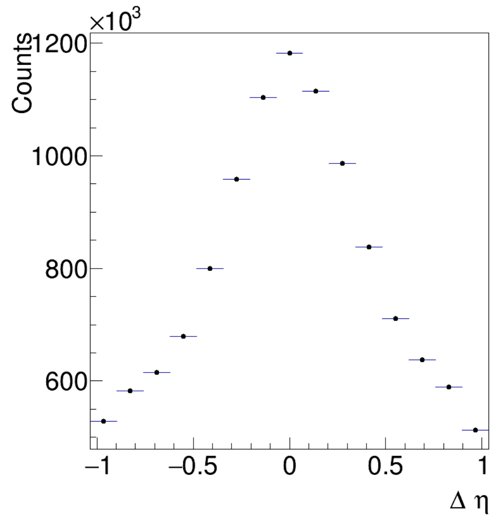

Figure 6.7: $\Delta\eta$ projection of signal distribution for for p–Φ correlation, ALICE pp collisions at $\sqrt{s_{NN}}$ = 13.6 TeV.

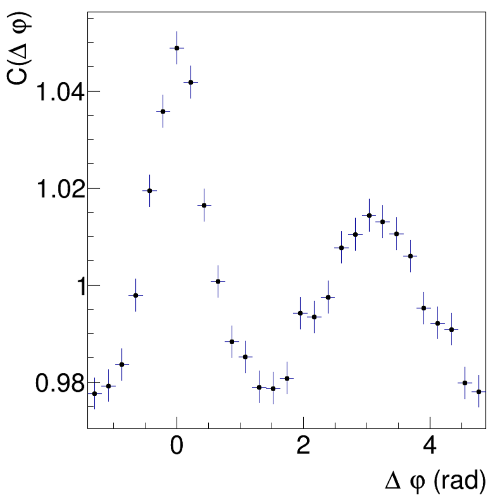

Figure 6.8: $\Delta\varphi$ projection of angular correlation function for p–Φ correlation, ALICE pp collisions at $\sqrt{s_{NN}}$ = 13.6 TeV.

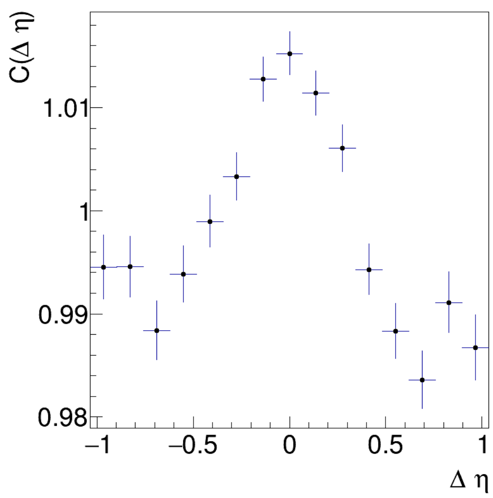

Figure 6.9: $\Delta\eta$ projection of angular correlation function for p–Φ correlation, ALICE pp collisions at $\sqrt{s_{NN}}$ = 13.6 TeV.

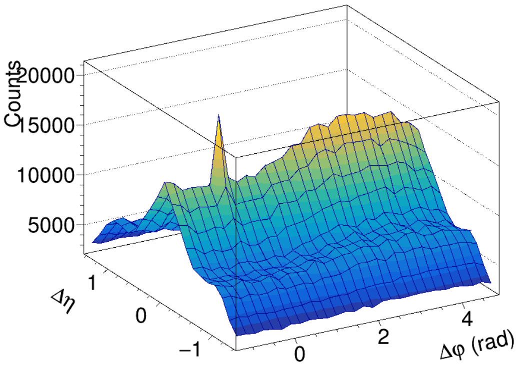

Figure 6.10: Signal distribution for p–p correlation, ALICE pp collisions at $\sqrt{s_{\mathrm{NN}}} = 13.6\,\mathrm{TeV}$.

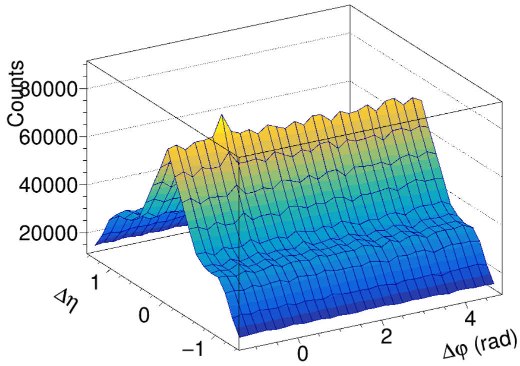

Figure 6.11: Background distribution for p–p correlation, ALICE pp collisions at $\sqrt{s_{\mathrm{NN}}} = 13.6\,\mathrm{TeV}$.

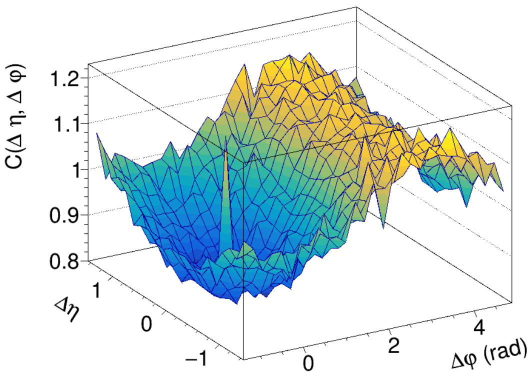

Figure 6.12: Angular correlation function for p–p correlation, ALICE pp collisions at $\sqrt{s_{\mathrm{NN}}} = 13.6\,\mathrm{TeV}$.

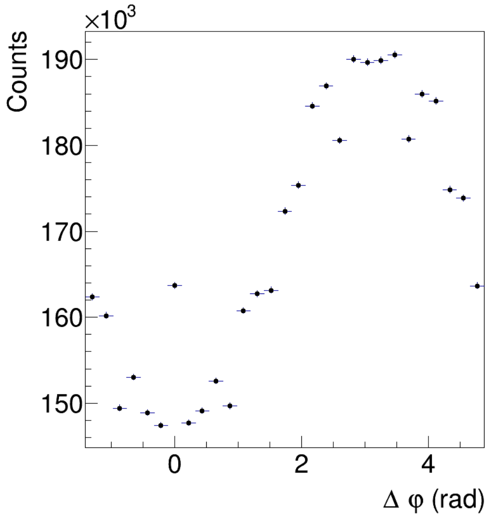

Figure 6.13: $\Delta\varphi$ projection of signal distribution for p–p correlation, ALICE pp collisions at $\sqrt{s_{\mathrm{NN}}} = 13.6\,\mathrm{TeV}$.

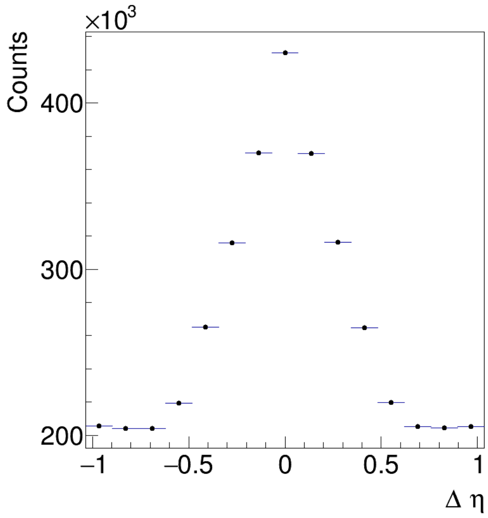

Figure 6.14: $\Delta\eta$ projection of signal distribution for p–p correlation, ALICE pp collisions at $\sqrt{s_{\mathrm{NN}}} = 13.6\,\mathrm{TeV}$.

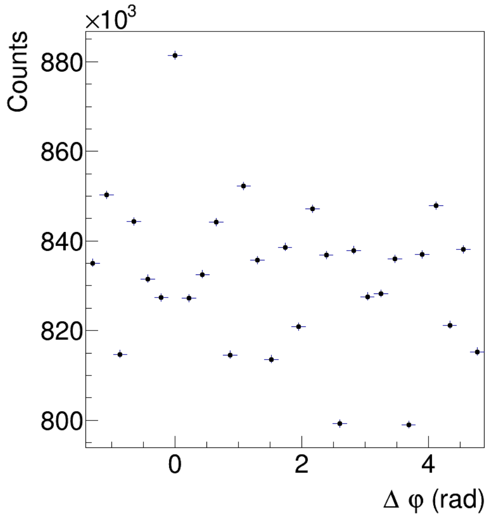

Figure 6.15: $\Delta\varphi$ projection of background distribution for p–p correlation, ALICE pp collisions at $\sqrt{s_{NN}}$ = 13.6 TeV.

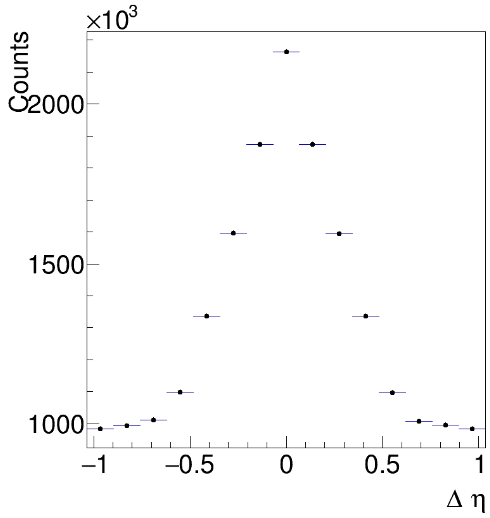

Figure 6.16: $\Delta\eta$ projection of signal distribution for for p–p correlation, ALICE pp collisions at $\sqrt{s_{NN}}$ = 13.6 TeV.

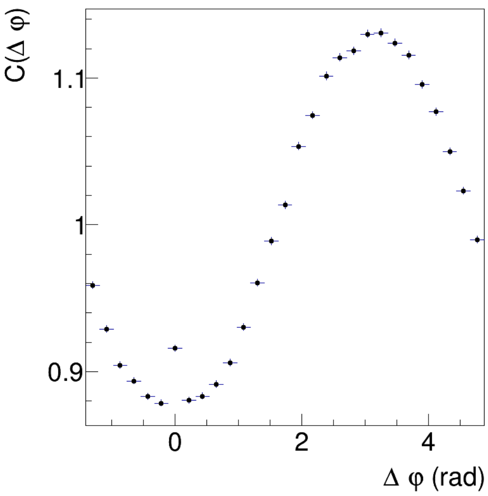

Figure 6.17: $\Delta\varphi$ projection of angular correlation function for p–p correlation, ALICE pp collisions at $\sqrt{s_{NN}}$ = 13.6 TeV.

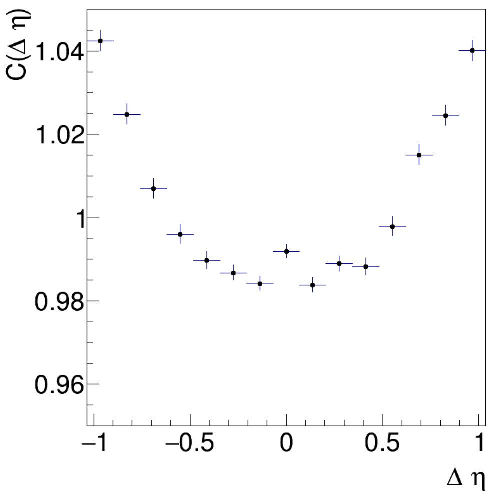

Figure 6.18: $\Delta\eta$ projection of angular correlation function for p–p correlation, ALICE pp collisions at $\sqrt{s_{NN}}$ = 13.6 TeV.

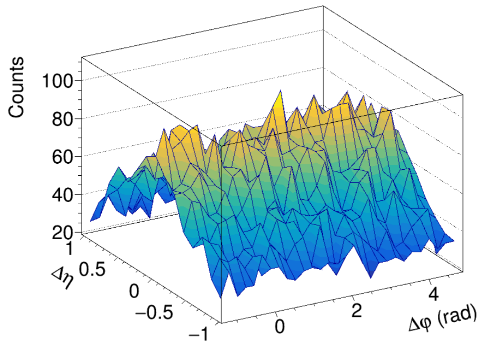

Figure 6.19: Signal distribution for p–Φ correlation, Pythia pp collisions at $\sqrt{s_{NN}}$ = 13.6 TeV.

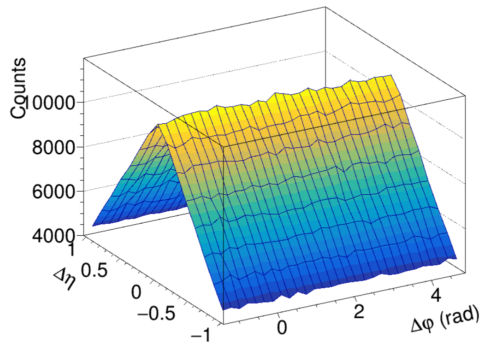

Figure 6.20: Background distribution for p–Φ correlation, Pythia pp collisions at $\sqrt{s_{NN}}$ = 13.6 TeV.

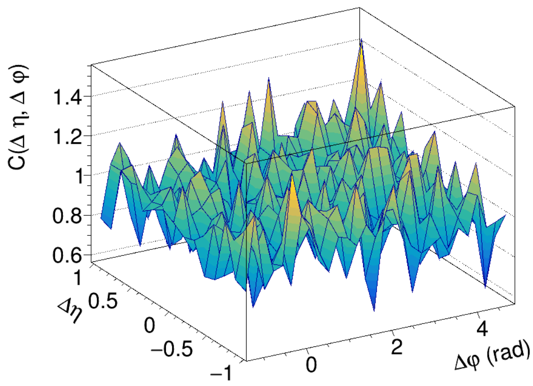

Figure 6.21: Angular correlation function for p–Φ correlation, Pythia pp collisions at $\sqrt{s_{NN}}$ = 13.6 TeV.

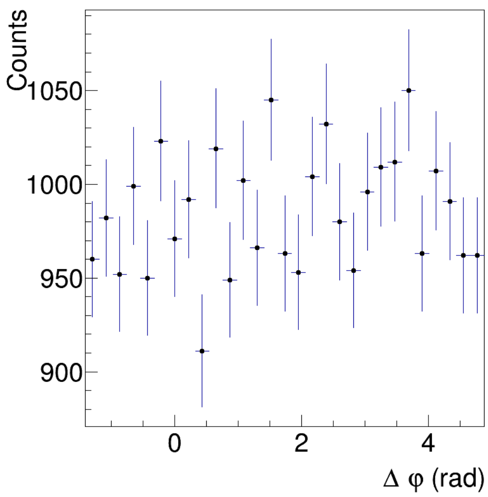

Figure 6.22: $\Delta\varphi$ projection of signal distribution for p–Φ correlation, Pythia pp collisions at $\sqrt{s_{NN}}$ = 13.6 TeV.

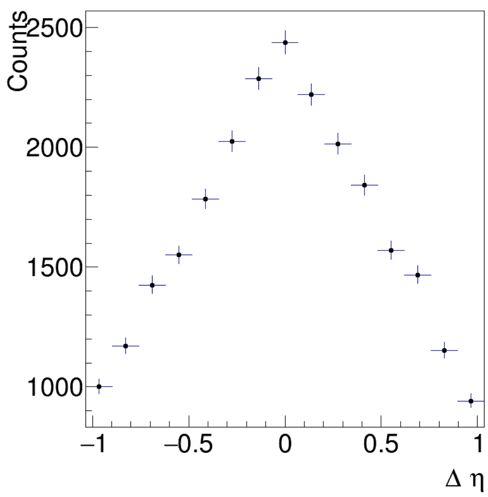

Figure 6.23: $\Delta\eta$ projection of signal distribution for p–Φ correlation, Pythia pp collisions at $\sqrt{s_{NN}}$ = 13.6 TeV.

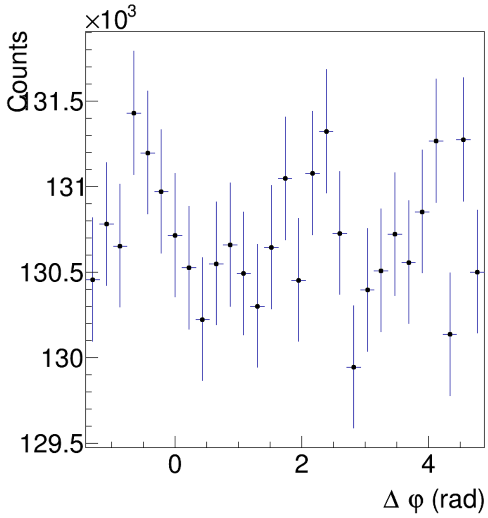

Figure 6.24: $\Delta\varphi$ projection of background distribution for p–Φ correlation, Pythia pp collisions at $\sqrt{s_{NN}}$ = 13.6 TeV.

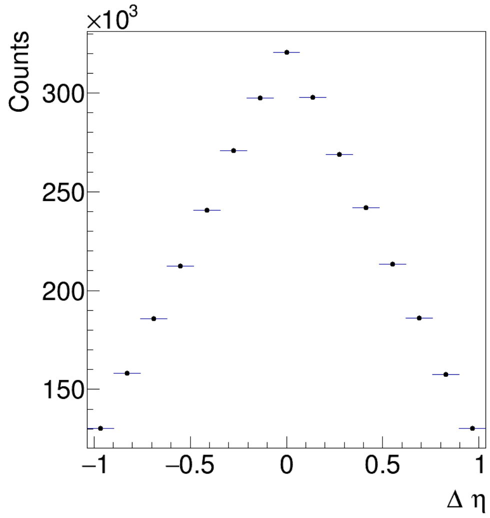

Figure 6.25: $\Delta\eta$ projection of signal distribution for for p–Φ correlation, Pythia pp collisions at $\sqrt{s_{NN}}$ = 13.6 TeV.

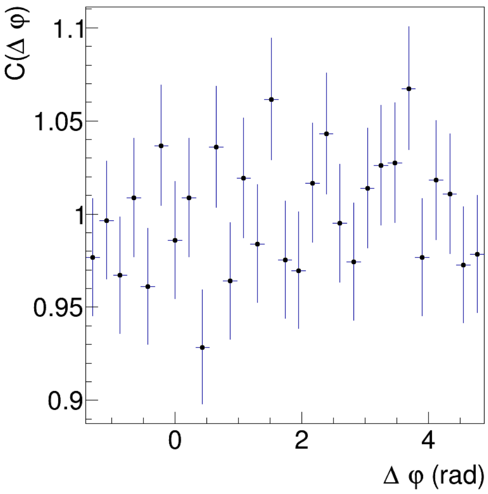

Figure 6.26: $\Delta\varphi$ projection of angular correlation function for p–Φ correlation, Pythia pp collisions at $\sqrt{s_{NN}}$ = 13.6 TeV.

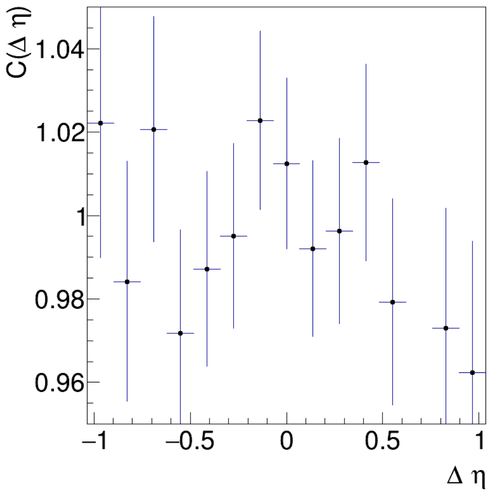

Figure 6.27: $\Delta\eta$ projection of angular correlation function for p–Φ correlation, Pythia pp collisions at $\sqrt{s_{NN}}$ = 13.6 TeV.

Chapter 7

Discussion of the results

In this section main results of this thesis are discussed. Figure 7.1 shows the angular correlation function for p–p correlation, whereas figure 7.2 shows the angular correlation function for p–Φ correlation. The anticorrelation seen in figure 7.1 can be understood in such a way that two protons relatively rarely appear close to each other in $\Delta\eta\Delta\varphi$ space. What this means is that multiple protons do not appear in a single jet. One can note that the results obtained for the p–p correlation agree with those obtained in the studies [7, 8] described in the theoretical introduction.

The result obtained for the p–Φ correlation indicates that the anti-correlation effect around the $(\Delta\eta, \Delta\varphi) = (0{,}0)$ point is not mass-related. This can be deduced from the fact that the Φ meson, despite its mass close to the proton, in the angular correlation p–Φ does not have an anticorrelation in the vicinity of the point $(\Delta\eta, \Delta\varphi) = (0{,}0)$. In contrast to the conclusions of the p–p angular correlation, the results of the p–Φ angular correlation makes it possible to observe that protons and Φ mesons can appear close to each other in $\Delta\eta\Delta\varphi$ space.

In figure 7.3 the comparison of the $\Delta\eta$ projection on the p–p correlation and p–Φ is presented. What can be seen is that the p–Φ correlation presents a completely different shape in contrast to the p–p correlation.

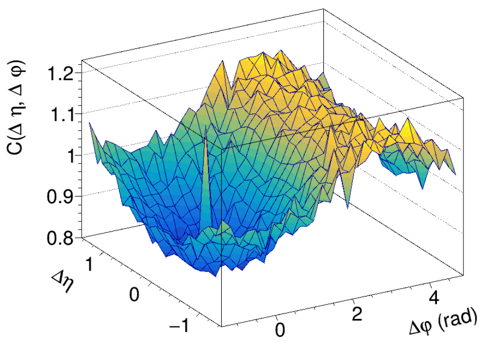

Figure 7.1: Angular correlation function for p–p correlation, ALICE pp collisions at $\sqrt{s_{NN}} = 13.6$ TeV.

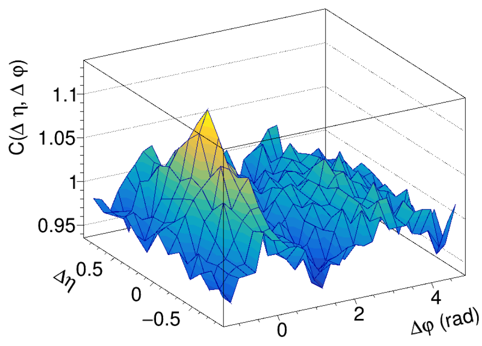

Figure 7.2: Angular correlation function for p–Φ correlation, ALICE pp collisions at $\sqrt{s_{NN}} = 13.6$ TeV.

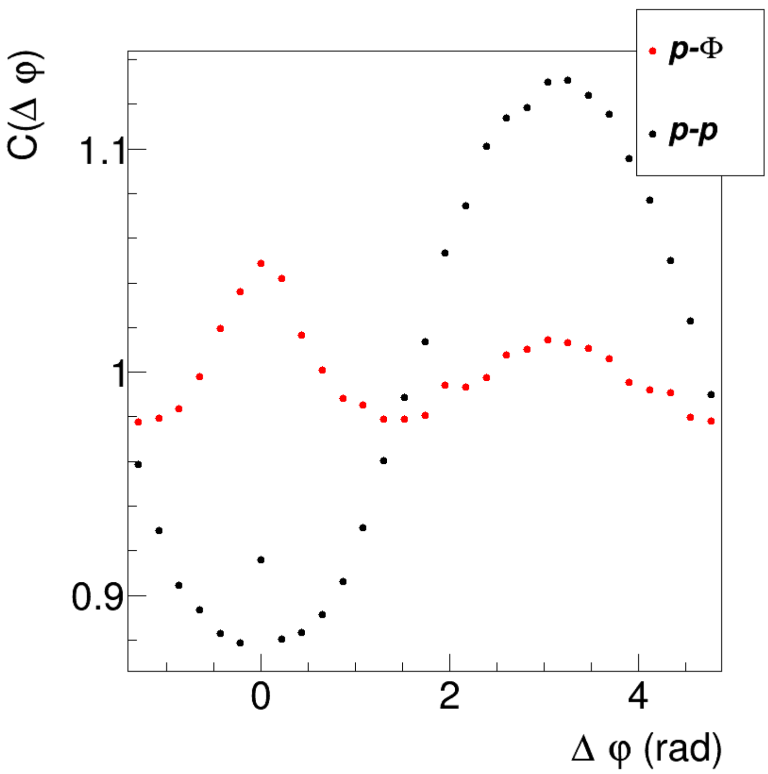

Figure 7.3: The comparison of the $\Delta\eta$ projection on the p–p correlation and p–Φ, ALICE pp collisions at $\sqrt{s_{NN}} = 13.6$ TeV.

Chapter 8

Summary and outlook

The new FemtoUniverse package, which I have been developing as part of my master's thesis, allows me to obtain results for p–p angular correlations that coincide with the experimental results previously obtained and analyzed in the introduction of this thesis. These results, which are a benchmark of the analysis performed, allow us to believe that the software does not contain errors that could negatively affect the analysis performed and that it is possible to compare correlations of baryons and mesons of similar mass.

The objective of this work was to obtain the angular correlation function for p–Φ correlation. I have achieved this goal and one can see that for pp collisions a peak is obtained in the vicinity of the $(\Delta\eta, \Delta\varphi)$ = (0,0) point. Additionally, the results of the analysis can help theoretical physicists improve the phenomenological models currently in use. The results, although preliminary, suggest an answer to the research hypothesis. Most likely, the anti-correlation effect is exclusively related to baryons. Meson correlations have no anti-correlation, so given this, it is most likely that baryons are produced differently than mesons. A systematic analysis, efficiency corrections, sideband analysis and Monte Carlo closure tests are planned for the study conducted in the future.

During my master's studies, I developed the FemtoUniverse package within the ALICE O^2 software. This package allows to perform hadron-Φ angular correlation analysis but furthermore allows the carrying out analyses of angular correlation functions or femtoscopic correlation studies for other particles. Currently, it is a package being developed both by a team from the Warsaw University of Technology, as well as by people from other universities around the world.

Bibliography

[1] K. Hattori, K. Itakura, and S. Ozaki. "Strong-field physics in QED and QCD: From fundamentals to applications". *Prog. Part. Nucl. Phys.*, 133:104068, 2023.

[2] R.D. Field and R.P. Feynman. "A parametrization of the properties of quark jets". *Nuclear Physics B*, 136(1):1–76, April 1978.

[3] C. Bierlich et al. ""A comprehensive guide to the physics and usage of PYTHIA 8.3". *SciPost Physics Codebases*, page 8, November 2022.

[4] Torbjorn Sjostrand, Stephen Mrenna, and Peter Z. Skands. PYTHIA 6.4 Physics and Manual. *JHEP*, 05:026, 2006.

[5] F.E. Paige et al., Isajet manual, https://www.nhn.ou.edu/~isajet/, accessed: 18.12.2023.

[6] G. Marchesini et al. "HERWIG 5.1 - a Monte Carlo event generator for simulating hadron emission reactions with interfering gluons". *Computer Physics Communications*, 67(3):465–508, 1992.

[7] **ALICE** collaboration, J. Adam, et al. Insight into particle production mechanisms via angular correlations of identified particles in pp collisions at $\sqrt{s} = 7$ TeV. *Eur. Phys. J. C*, 77(8):569, 2017. [Erratum: Eur.Phys.J.C 79, 998 (2019)].

[8] **STAR Collaboration** J. Adam et al. "Beam-energy dependence of identified two-particle angular correlations in $\sqrt{s_{NN}} = 7.7 - 200$ GeV AuAu collisions". *Phys. Rev. C*, 101:014916, Jan 2020.

[9] T. Sjöstrand. "Collective Effects: the viewpoint of HEP MC codes". *Nuclear Physics A*, 982:43–49, 2019. The 27th International Conference on Ultrarelativistic Nucleus-Nucleus Collisions: Quark Matter 2018.

[10] N. Demazure, V. Sebastián, and F. Llanes-Estrada. "Baryon Anticorrelations in PYTHIA". *Few-Body Systems*, 64, 07 2023.

[11] L. Lönnblad and H. Shah. "Baryon correlations in Pythia". *Eur. Phys. J. C*, 83(12):1105, 2023.

[12] *About | CERN* – https://home.cern/about, accessed: 28.07.2023.

[13] **ATLAS** collaboration, G. Aad, et al. "Observation of a new particle in the search for the Standard Model Higgs boson with the ATLAS detector at the LHC". *Phys. Lett. B*, 716:1–29, 2012.

[14] *Information Management: A Proposal* Tim Berners-Lee, CERN – https://cds.cern.ch/record/369245/files/dd-89-001.pdf, access: 05.01.2024.

[15] A. P. Jeavons et al. "A High Resolution Proportional Chamber Positron Camera and its applications". *IEEE Trans. Nucl. Sci.*, 25:164–173, 1978.

[16] M. Vretenar et al. "The next ion medical machine study at CERN: Towards a next generation cancer research and therapy facility with ion beams". *JACoW*, IPAC2021:MOPAB413, 2021.

[17] L. Evans and P. Bryant. "LHC machine". *Journal of Instrumentation*, 3(08):S08001, aug 2008.

[18] *Largest machine | Guinness world records* – https://www.guinnessworldrecords.com/world-records/103591-largest-machine, accessed: 31.07.2023.

[19] E. Lopienska. "The CERN accelerator complex, layout in 2022. Complexe des accélérateurs du CERN en janvier 2022". 2022. General Photo.

[20] K. **ALICE collaboration** Aamodt et al. "The ALICE experiment at the CERN LHC". *JINST*, 3:S08002, 2008.

[21] K. Rajagopal and F. Wilczek. *"The Condensed matter physics of QCD"*, pages 2061–2151. 11 2000.

[22] S. Siddhanta. "ALICE Run 3 at the LHC". In *2023 IEEE Nuclear Science Symposium, Medical Imaging Conference and International Symposium on Room-Temperature Semiconductor Detectors (NSS MIC RTSD)*, pages 1–1, 2023.

[23] *ALICE upgrades during LS2* – https://home.cern/press/2022/ALICE-upgrades-LS2, accessed: 05.08.2023.

[24] Arturo Tauro. ALICE Schematics. General Photo, 2017.

[25] *WUT CERN group* – https://twiki.cern.ch/twiki/bin/view/Main/WutStudents, accessed:.

[26] *ALICE FIT* – https://alice-collaboration.web.cern.ch/menu_proj_items/FIT, accessed 03.08.2023.

[27] **ALICE** collaboration and C. Lippmann. "Upgrade of the ALICE Time Projection Chamber". 3 2014.

[28] **ALICE** collaboration, G. Dellacasa, et al. "ALICE technical design report of the time-of-flight system (TOF)". 2 2000.

[29] W. H. Trzaska. "New ALICE detectors for Run 3 and 4 at the CERN LHC". *Nuclear Instruments and Methods in Physics Research Section A: Accelerators, Spectrometers, Detectors and Associated Equipment*, 958:162116, 2020. Proceedings of the Vienna Conference on Instrumentation 2019.

[30] ALICE TOF, https://alice-collaboration.web.cern.ch/menu_proj_items/tof, accessed: 23.12.2023.

[31] **ALICE** collaboration and D. Colella. "ALICE ITS upgrade for LHC Run 3: commissioning in the laboratory". *J. Phys. Conf. Ser.*, 2374(1):012058, 2022.

[32] P. Buncic, M. Krzewicki, and P. Vande Vyvre. "Technical Design Report for the Upgrade of the Online-Offline Computing System". 4 2015.

[33] *Appache Arrow | A cross-language development platform for in-memory analytics* – https://arrow.apache.org/, accessed: 05.01.2024.

[34] R. Quishpe, J. F. Grosse-oetringhaus, R. Cruceru, and C. Grigoras. "Hyperloop – The ALICE analysis train system for Run 3". *PoS*, LHCP2021:250, 2021.

[35] D. Britton and S. Lloyd. "How to deal with petabytes of data: The LHC Grid project". *Reports on Progress in Physics*, 77:065902, 06 2014.

[36] *The Worldwide LHC Computing Grid (WLCG) | CERN* – https://home.cern/science/computing/grid, accessed: 10.08.2023.

[37] WLCG Worldwide LHC Computing Grid – Monitoring Visualisation – https://wlcg.web.cern.ch/using-wlcg/monitoring-visualisation, accessed: 27.12.2023.

[38] M. Janik. *"Two-particle correlations as a function of relative azimuthal angle and pseudorapidity in proton-proton collisions registered by the ALICE experiment "*. CERN-THESIS-2014-339, 2014.

[39] Ł. K Graczykowski and M. A. Janik. "Unfolding the effects of final-state interactions and quantum statistics in two-particle angular correlations". *Phys. Rev. C*, 104(5):054909, 2021.

[40] **Particle Data Group** collaboration and M. Tanabashi et al. "Review of Particle Physics". *Phys. Rev. D*, 98:030001, Aug 2018.

[41] Φ meson (1020) - Particle Data Group page: https://pdglive.lbl.gov/Particle.action?node=M004&init=0&home=MXXX005, accessed 23.12.2023.

[42] C. Cavicchioli. *"Development and Commissioning of the Pixel Trigger System for the ALICE Experiment at the CERN Large Hadron Collider"*. PhD thesis, 01 2010.

List of Figures

List of Tables

Appendix A

Glossary

A.1. Choice of observables

Figure A.1 depicts ALICE detector coordinate system. The Z-axis was taken as the axis along the beam, while the X and Y axes are in a plane perpendicular to the beam axis.

A.1.1. Polar angle θ

Polar angle θ is an angle between particle momentum and the beam axis.

A.1.2. Pseudorapidity η

Pseudorapidity is defined as a function of the polar angle θ as:

$$\eta = -\ln \frac{\theta}{2} \tag{A.1}$$

The differences in pseudorapidity ($\Delta\eta$) are invariant with respect to the Lorentz transformation and the particle production is constant as a function of rapidity. Pseudorapidity does not require knowledge of particle mass, so pseudorapidity analyses do not mandate that the detectors used can measure mass. Because of that, to perform studies in the field of high-energy physics pseudorapidity is often used.

A.1.3. Transverse momentum $\vec{p_T}$

Transverse momentum $\vec{p_T}$ is the particle momentum that is perpendicular to the beam axis. It is defined as follows:

$$\vec{p_T} = [p_x, p_y] \tag{A.2}$$

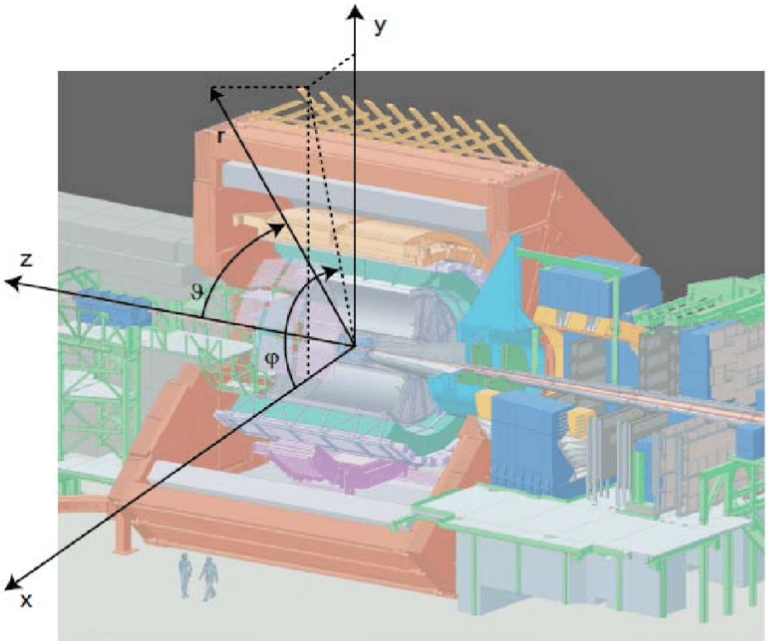

Figure A.1: ALICE coordinate system [42].

A.1.4. Azimuthal angle φ

Azimuthal angle φ is an angle between the transverse momentum of the particle p_T and the positive x-axis.

Appendix B

Invariant mass

Figures B.1 - B.10 show invariant mass distribution for Φ meson in different p_T ranges. As a background function, a second-degree polynomial was chosen, whereas, for the signal function, the Lorentzian peak was selected. The graph B.11, on the other hand, provides the value of purity as a function of transverse momentum p_T.

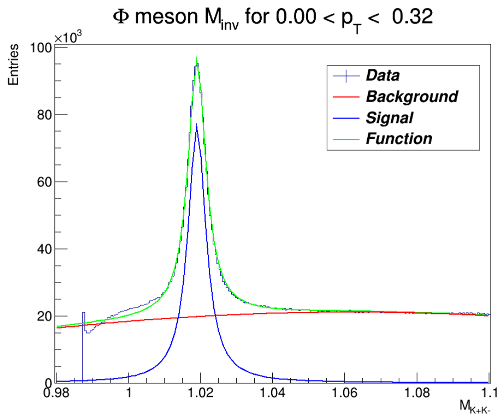

Figure B.1: Invariant mass distribution for the $0.00\,\mathrm{GeV/c} < p_T < 0.32\,\mathrm{GeV/c}$.

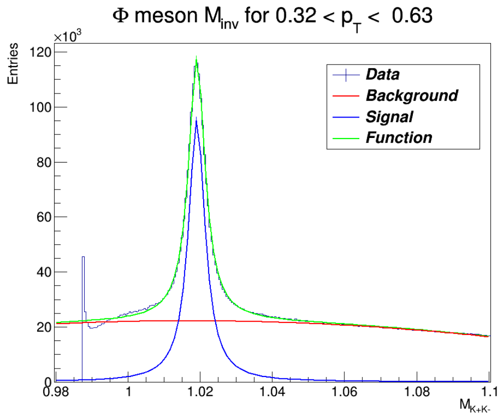

Figure B.2: Invariant mass distribution for the $0.32\,\mathrm{GeV/c} < p_T < 0.63\,\mathrm{GeV/c}$.

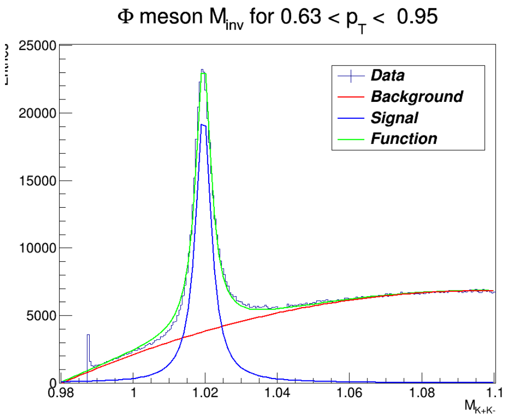

Figure B.3: Invariant mass distribution for the 0.63 GeV/c $< p_T <$ 0.95 GeV/c.

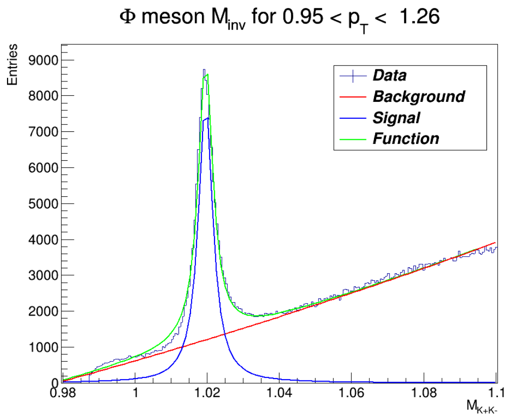

Figure B.4: Invariant mass distribution for the 0.95 GeV/c $< p_T <$ 1.26 GeV/c.

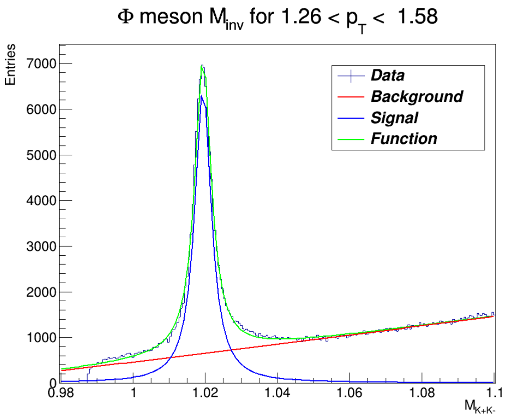

Figure B.5: Invariant mass distribution for the 1.26 GeV/c $< p_T <$ 1.58 GeV/c.

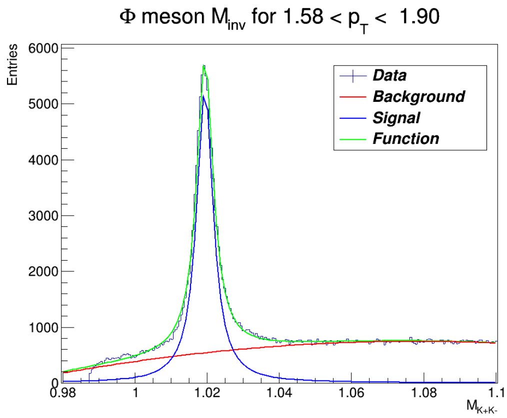

Figure B.6: Invariant mass distribution for the 1.58 GeV/c $< p_T <$ 1.90 GeV/c.

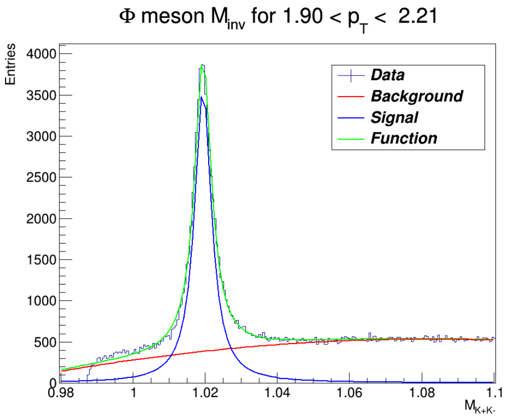

Figure B.7: Invariant mass distribution for the 1.90 GeV/c $< p_T <$ 2.21 GeV/c.

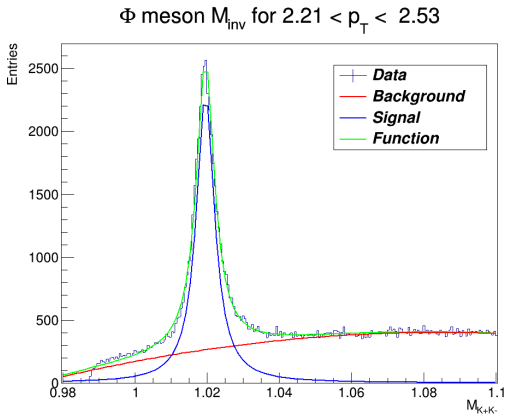

Figure B.8: Invariant mass distribution for the 2.21 GeV/c $< p_T <$ 2.53 GeV/c.

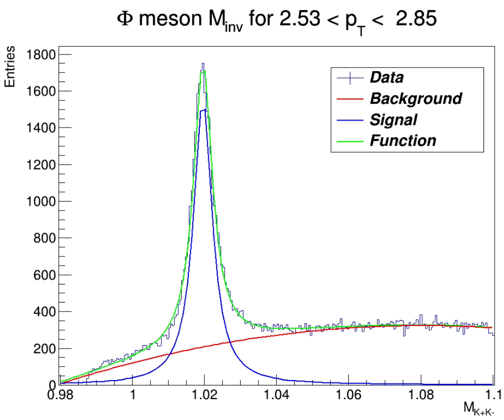

Figure B.9: Invariant mass distribution for the 2.53 GeV/c $< p_{\mathrm{T}} <$ 2.85 GeV/c.

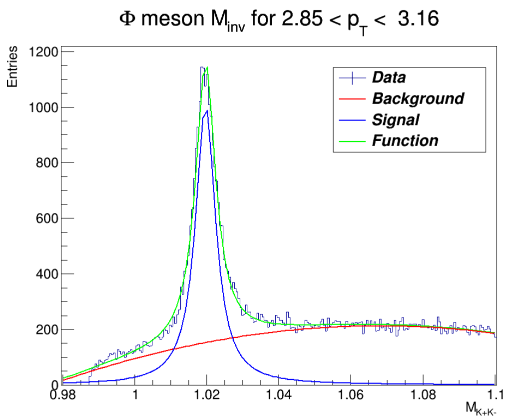

Figure B.10: Invariant mass distribution for the 2.85 GeV/c $< p_{\mathrm{T}} <$ 3.16 GeV/c.

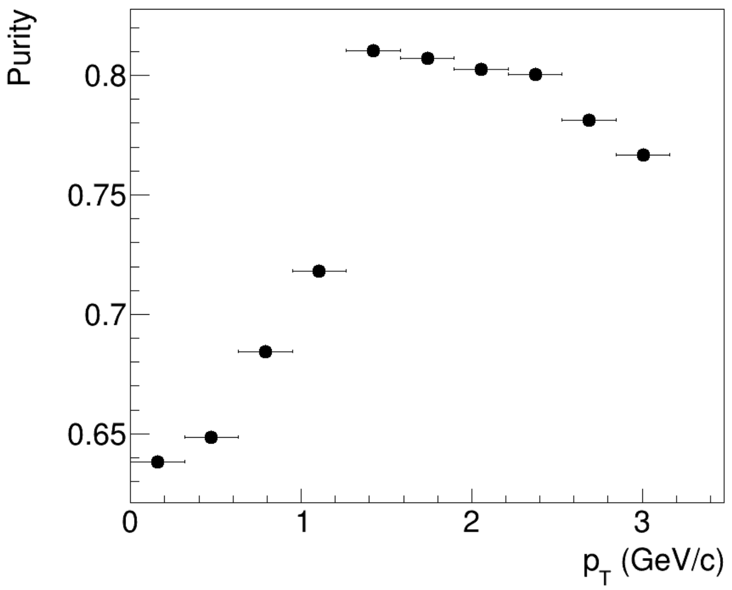

Figure B.11: Purity vs p_{T} for Φ meson candidates.

Appendix C

Two tracks selection criteria

Figures C.1 and C.2 show $\Delta\eta\Delta\varphi^*$ distributions for p–K^+ and p–K^- pairs, whereas figures C.3 - C.6 present the zoomed $\Delta\eta\Delta\varphi^*$ distributions for p–K^+ and p–K^-, respectively. The selection used in this analysis has the following form: $|\Delta\eta| < 0.004 \wedge |\Delta\varphi^*| < 0.015$. During the writing of this thesis, $\Delta\eta\Delta\varphi^*$ graphs were constructed as the sum of pairs derived from the same events and mixed events. In a later stage of the work, it is planned to divide the graphs of the plot obtained from correlating pairs originating from the same events by plot derived from pairs from mixed events.

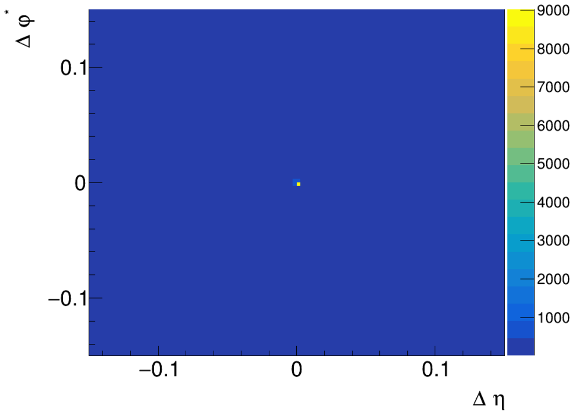

Figure C.1: $\Delta\eta\Delta\varphi^{*}$ distribution for pK^{+} before the selection, ALICE pp collisions at $\sqrt{s_{\mathrm{NN}}} = 13.6\,\mathrm{TeV}$.

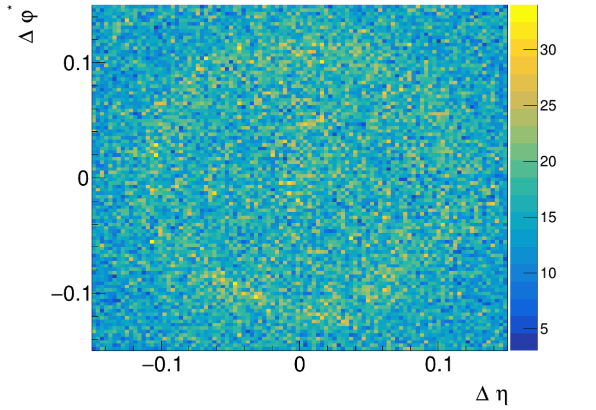

Figure C.2: $\Delta\eta\Delta\varphi^{*}$ distribution for pK^{-} before the selection, ALICE pp collisions at $\sqrt{s_{\mathrm{NN}}} = 13.6\,\mathrm{TeV}$.

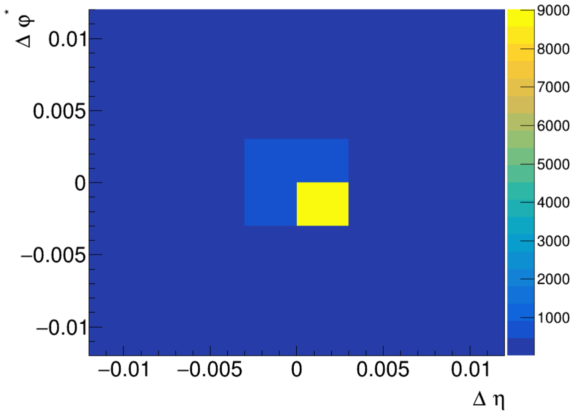

Figure C.3: $\Delta\eta\Delta\varphi^{*}$ distribution for pK^{+} before the selection, ALICE pp collisions at $\sqrt{s_{\mathrm{NN}}} = 13.6\,\mathrm{TeV}$ (zoomed).

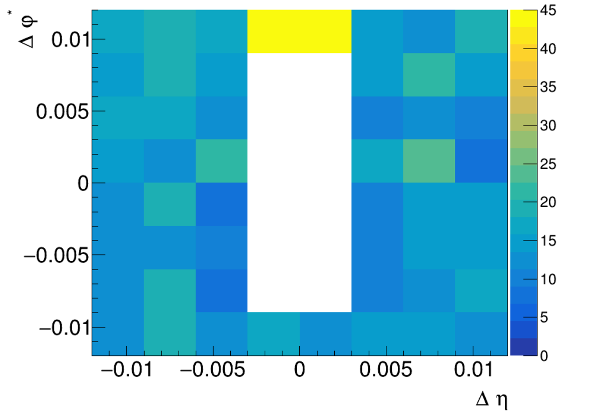

Figure C.4: $\Delta\eta\Delta\varphi^{*}$ distribution for pK^{+} after the selection, ALICE pp collisions at $\sqrt{s_{\mathrm{NN}}} = 13.6\,\mathrm{TeV}$ (zoomed).

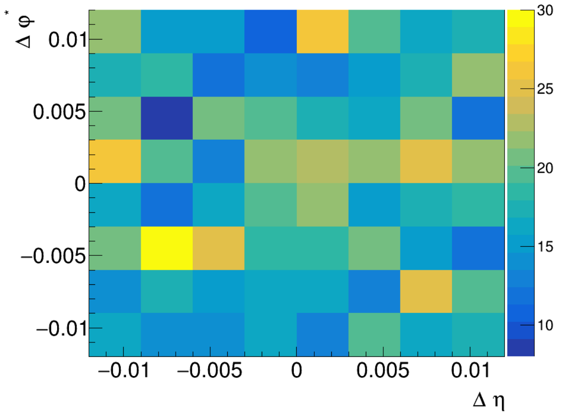

Figure C.5: $\Delta\eta\Delta\varphi^{*}$ distribution for pK^{-} before the selection, ALICE pp collisions at $\sqrt{s_{\mathrm{NN}}} = 13.6\,\mathrm{TeV}$ (zoomed).

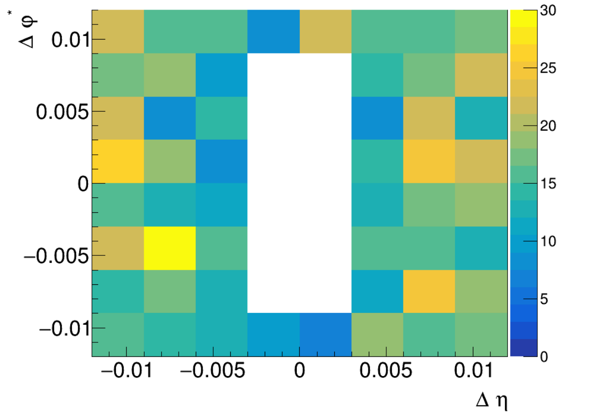

Figure C.6: $\Delta\eta\Delta\varphi^{*}$ distribution for pK^{-} after the selection, ALICE pp collisions at $\sqrt{s_{\mathrm{NN}}} = 13.6\,\mathrm{TeV}$ (zoomed).

Appendix D

Angular correlation study for $\pi^+ - \pi^+$

D.1. Data analysis

Angular correlation analysis for $\pi^+ - \pi^+$ was performed as a benchmark. In the D.1 pion selection criteria are listed. Figures D.1 - D.6 show signal, background and angular correlation function and their projections on the $\Delta\varphi$ axis.

D.2. MC Truth analysis

Figures D.7 - D.12 show signal, background and angular correlation function and their projections on the $\Delta\varphi$ axis.

Table D.1: Pion selection criteria.

Selection criteria	**Value**
Transverse momentum	$p_T \in (0.1; 2.5)$ GeV
Pseudorapidity	$\|\eta\| < 0.8$
IsGlobalTrack	True
Particle Identification	$\|n_{\sigma,\mathrm{TPC}}\| < 3.0$ for $p < 0.3$ GeV/c
	$\|n_{\sigma,\mathrm{TPC}}\| < 3.0$ and $\|n_{\sigma,\mathrm{TOF}}\| < 3.0$ for $p < 0.3$ GeV/c

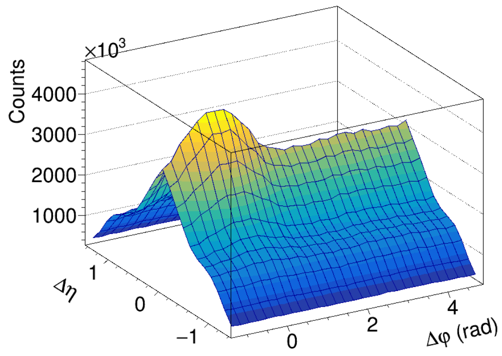

Figure D.1: Signal distribution for $\pi^+ - \pi^+$ correlation, ALICE pp collisions at $\sqrt{s_{NN}} = 13.6\,\mathrm{TeV}$.

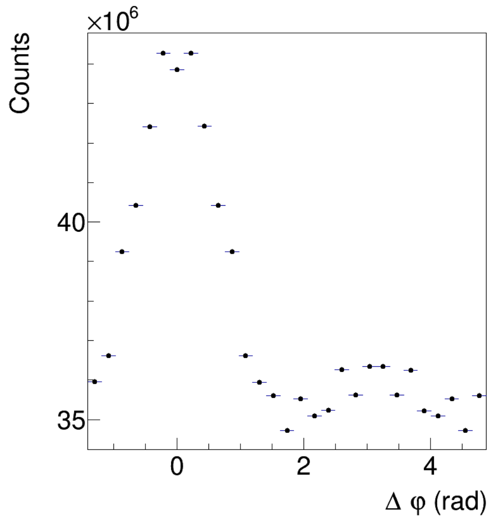

Figure D.2: $\Delta\varphi$ projection of signal distribution for $\pi^+ - \pi^+$ correlation, ALICE pp collisions at $\sqrt{s_{NN}} = 13.6\,\mathrm{TeV}$.

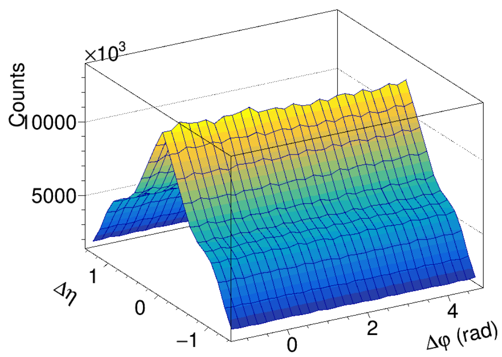

Figure D.3: Background distribution for $\pi^+ - \pi^+$ correlation, ALICE pp collisions at $\sqrt{s_{NN}} = 13.6\,\mathrm{TeV}$.

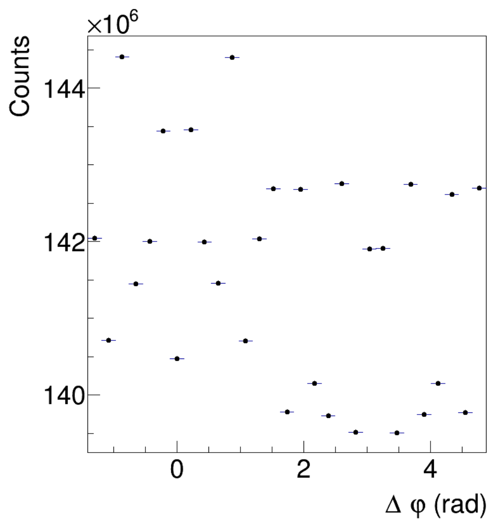

Figure D.4: $\Delta\varphi$ projection of background distribution for $\pi^+ - \pi^+$ correlation, ALICE pp collisions at $\sqrt{s_{NN}} = 13.6\,\mathrm{TeV}$.

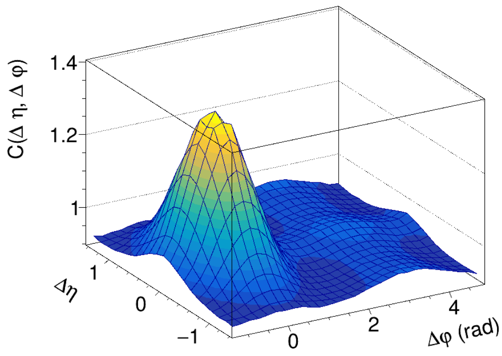

Figure D.5: Angular correlation function for $\pi^+ - \pi^+$ correlation, ALICE pp collisions at $\sqrt{s_{\text{NN}}}$ = 13.6 TeV.

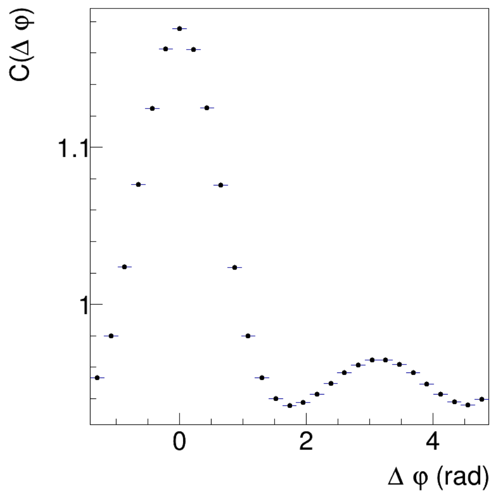

Figure D.6: $\Delta\varphi$ projection of angular correlation function for $\pi^+ - \pi^+$ correlation, ALICE pp collisions at $\sqrt{s_{\text{NN}}}$ = 13.6 TeV.

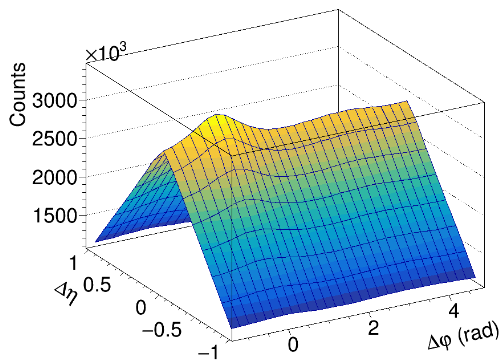

Figure D.7: Signal distribution for $\pi^+ - \pi^+$ correlation, Pythia pp collisions at $\sqrt{s_{\text{NN}}}$ = 13.6 TeV.

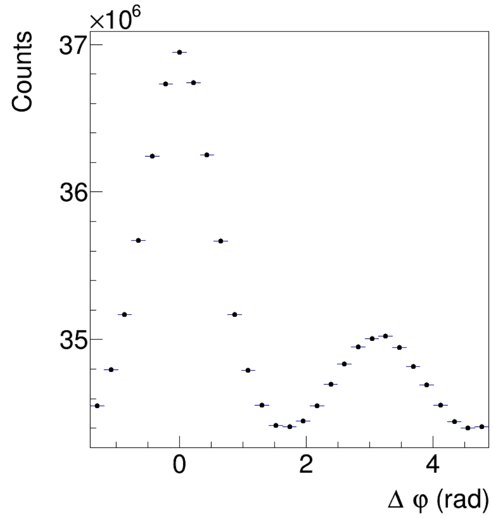

Figure D.8: $\Delta\varphi$ projection of signal distribution for $\pi^+ - \pi^+$ correlation, Pythia pp collisions at $\sqrt{s_{\text{NN}}}$ = 13.6 TeV.

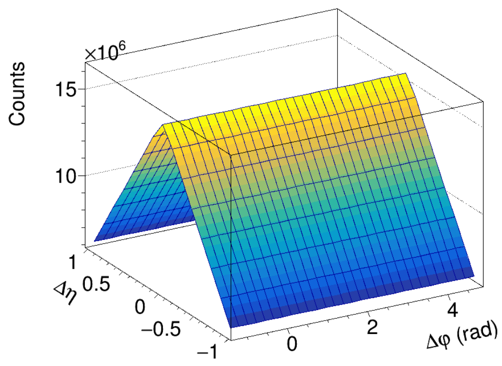

Figure D.9: Background distribution for $\pi^+ - \pi^+$ correlation, Pythia pp collisions at $\sqrt{s_{\mathrm{NN}}} = 13.6$ TeV.

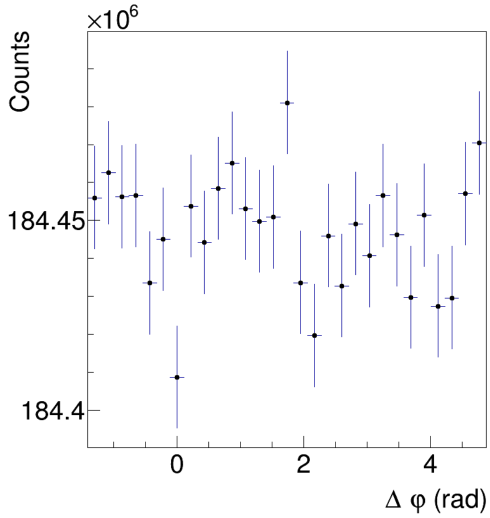

Figure D.10: $\Delta\varphi$ projection of background distribution for $\pi^+ - \pi^+$ correlation, Pythia pp collisions at $\sqrt{s_{\mathrm{NN}}} = 13.6$ TeV.

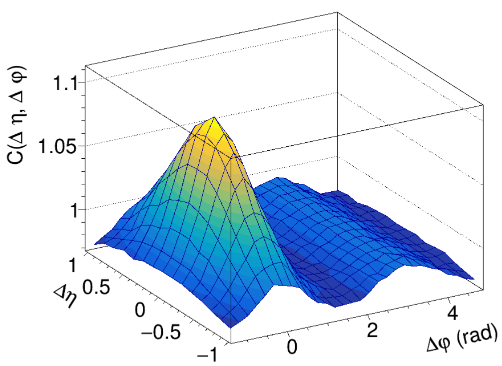

Figure D.11: Angular correlation function for $\pi^+ - \pi^+$ correlation, Pythia pp collisions at $\sqrt{s_{\mathrm{NN}}} = 13.6$ TeV.

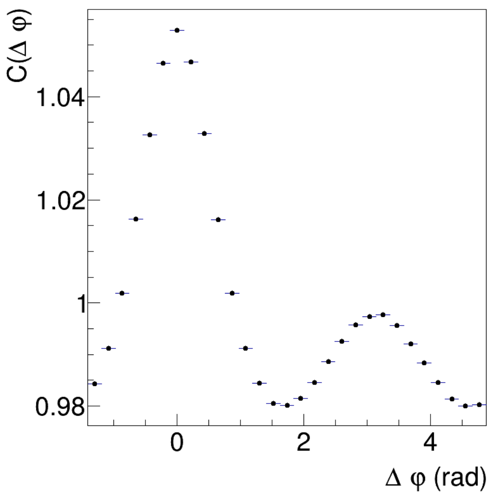

Figure D.12: $\Delta\varphi$ projection of angular correlation function for $\pi^+ - \pi^+$ correlation, Pythia pp collisions at $\sqrt{s_{\mathrm{NN}}} = 13.6$ TeV.